Coupling the TKE-ACM2 Planetary Boundary Layer Scheme with the Building Effect Parameterization Model

Wanliang Zhang[1], Chao Ren[2], Edward Yan Yung Ng[3], Michael Mau Fung Wong[1], and Jimmy Chi Hung Fung[1,4]

[1]Division of Environment and Sustainability, Hong Kong University of Science and Technology, Hong Kong, China
[2]Division of Landscape Architecture, Department of Architecture, Faculty of Architecture, University of Hong Kong, Hong Kong, China
[3]School of Architecture, The Chinese University of Hong Kong, Shatin NT, Hong Kong, China
[4]Department of Mathematics, Hong Kong University of Science and Technology, Hong Kong, China

Correspondence: Jimmy Chi Hung Fung (majfung@ust.hk)

Abstract. Understanding and modeling the turbulent transport of surface layer fluxes ~~plays a critical role in a~~ are essential for numerical weather forecasting ~~model~~models. The presence of heterogeneous surface obstacles (buildings) that have dimensions comparable to the model vertical resolution requires further complexity and design in the planetary boundary layer (PBL) scheme. In this study, we develop ~~the~~ a numerical method to couple ~~one of the~~ a recently validated PBL ~~schemes~~scheme, TKE-ACM2, with ~~the~~ multi-layer Building Effect Parameterization (BEP) ~~model in WRF~~in the Weather Research and Forecasting (WRF) model. Subsequently, the performance of TKE-ACM2+BEP ~~has been~~ is examined under idealized convective atmospheric conditions with a simplified building layout. Furthermore, its reproducibility is benchmarked with ~~one of the~~ a state-of-the-art large-eddy simulation ~~models~~model, PALM, which ~~can explicitly resolve~~ explicitly resolves the building aerodynamics. The ~~result indicates~~ results indicate that TKE-ACM2+BEP outperforms ~~the other~~ another operational PBL scheme (Boulac) coupled with BEP by reducing ~~the~~ bias in both the potential temperature (θ) and wind speed (u). Following this, real case simulations are conducted for a highly urbanized domain, ~~i.e.,~~ namely the Pearl River Delta (PRD) region in China. ~~The high-resolution~~ High-resolution wind speed LiDAR observations suggest that TKE-ACM2+BEP ~~can mitigate the~~ reduces overestimation in the lower part of the boundary layer compared ~~to~~ with the Bulk method, which lacks an urban scheme, at a LiDAR site located in a densely built environment. In addition, the surface temperature and relative humidity ~~can be improved in~~ given by TKE-ACM2+BEP at surface stations in urbanized areas ~~compared to~~ are more accurate than those given by TKE-ACM2 without BEP. However, it is revealed that BEP ~~may not always imply a better reproduction of~~ does not always improve the accuracy of the surface wind speed~~as it could exert~~, as it can introduce excessive aerodynamic drag.

1 Introduction

Urbanization is a ubiquitous phenomenon that is widely seen across the globe. The unprecedented rate of urbanization ~~results~~ has resulted in more structures being constructed in populated cities, complicating the response of ~~the~~ incoming airflow when it encounters building clusters in the urban canopy layer (UCL) and the overlying roughness sub-layer~~(RSL)~~, or RSL (Rotach, 1999). This RSL is characterized by strong turbulence due to the presence of buildings ~~which separates~~ that separate the mean airflow and ~~forms~~ form the wake region (Cleugh and Grimmond, 2012), and ~~has significant impacts on~~ affect the vertical transport of momentum and scalars over urban regions (Roth, 2000). ~~Parameterizations of~~ Mesoscale numerical weather prediction models require parameterizations to account for the net sub-grid effects ~~imposed by the~~ of building obstacles in ~~the~~ heavily populated cities~~are necessary for the mesoscale numerical weather prediction models given~~. Given that their horizontal resolution is typically ~~10-50 times larger than~~ 10 to 50 times the street canyon scale (Britter and Hanna, 2003)~~which is unable to resolve the aerodynamicsexplicitly~~, they cannot explicitly resolve urban aerodynamics. In the widely-used Weather Research and Forecasting (WRF) model (Skamarock et al., 2019), the surface shear stress exerted by any type of ground obstacle can be simply parameterized using ~~the~~ well-known Monin-Obukhov similarity theory (MOST) by defining a friction velocity, u_*, ~~which~~ in what is known as the "Bulk" scheme (Liu et al., 2006). Studies have ~~been carried out to determine~~ determined different roughness lengths, z_0, a prerequisite for u_*, to account for the heterogeneity of land type (Davenport et al., 2000). However, the Bulk scheme has certain limitations, such as poorly ~~represented~~ representing urban geometry and ~~inadequacy of applying MOST when applied to the whole RSL (Rotach, 1993), albeit it~~ failing to apply MOST across the entire RSL (Rotach, 1993). Yet the Bulk scheme is commonly used for real-time weather forecasts (Liu et al., 2006) and analyzing the effects of built-up ~~lands on land-see~~ land on land-sea breeze circulations (Lo et al., 2007).

The single-layer urban canopy model (SLUCM) ~~(Kusaka et al., 2001; Kusaka and Kimura, 2004)~~ pioneered by Kusaka et al. (2001); Ku is a moderately complex urban parameterization scheme in ~~WRF~~ the WRF model that considers the exchange of momentum and energy between the three-dimensional urban surfaces ~~with~~ and the atmosphere in ~~the~~ idealized infinitely long street canyons. ~~One remarkable drawback of~~ A major drawback of the SLUCM is that only the first model layer experiences the momentum and sensible heat fluxes ~~(F_i for $i \in \{1\}$, where i is the vertical index at the model center)~~ due to the presence of buildings, which ~~could~~ may lead to unrealistically predicted prognostic variables in the upper surface layer over regions of medium- to high-rise building ~~cluster regions~~clustering, such as the Pearl River Delta (PRD) region in southern China. In contrast, ~~the~~ multi-layer urban canopy models, such as the Building Effects Parameterizations (Martilli et al., 2002, BEP), and BEP coupled ~~to~~ with the Building Energy Model (Salamanca and Martilli, 2010, BEP+BEM), ~~are of~~ have a higher hierarchy in urban ~~effects~~ effect parameterizations because of their ~~capabilities in recognizing the vertically varied~~ ability to recognize vertically varying interactions between the atmosphere and buildings (Chen et al., 2011)~~, i.e., F_i for $i \in \{1, I_{UCL}\}$, where I_{UCL} is the maximum probable vertical index within UCL~~. Besides the direct ~~impact~~ effect of buildings on the atmosphere dynamics and thermodynamics, BEP/BEP+BEM offer modifications to two length scales in the dissipation term of the prognostic turbulent kinetic energy (TKE) equation ~~are offered by BEP/ BEP+BEM~~ (Martilli et al., 2002) to account for the altered ~~vortexes'~~ vortex size. Studies ~~reveal~~ have revealed that meteorological fields and urban heat island ~~circulation~~ effects can be better reproduced ~~utilizing the~~ using BEP/BEP+BEM ~~models~~ worldwide, such as in Hong Kong (Wang et al., 2017), Barcelona (Ribeiro et al., 2021), and Bolzano (Pappaccogli et al., 2021).

However, multi-layer BEP/BEP+BEM models are ~~not practiced as ubiquitously as~~ adopted less widely than the Bulk scheme or ~~the~~ SLUCM because they ~~work with~~ have only been tentatively coupled to a few planetary boundary layer (PBL) schemes [e.g., Boulac (Bougeault and Lacarrere, 1989), MYJ (Janjić, 1994), and YSU (Hong et al., 2006) added ~~by Hendricks et al. (2020)~~

~~recently~~recently by Hendricks et al. (2020)]. ~~Considering~~ This is primarily due to the challenges associated with incorporating the transformation of mean kinetic energy into TKE within a first-order closure PBL scheme, such as the YSU scheme. As a result, the eddy diffusivity can only be adjusted in response to surface fluxes, limiting its ability to account for the generation and dissipation of TKE through other boundary layer processes, such as the generation of TKE by wind shear and buoyancy. Additionally, the other two PBL schemes (MYJ and Boulac) model the vertical mixing of momentum between two adjacent layers, but lack the non-local mixing driven by large-scale eddies under convective conditions. For instance, Coniglio et al. (2013) reported that MYJ produces PBLs that are too shallow and moist PBLs in the evening, and Xie et al. (2012) found that the PBL height diagnosed by Boulac may be too short to be realistic. Considering that particular PBL schemes may be preferable for different regional and seasonal simulations (García-Díez et al., 2013), there is a need to couple BEP/BEP+BEM with other WRF PBL schemes (Martilli et al., 2009), especially a scheme featuring a non-local transport component under convective conditions.

PBL schemes that redistribute ~~the~~ surface fluxes and calculate ~~the vertical mixing have profound effects on accurately depicting the~~ vertical mixing are important to the accurate depiction of meteorological conditions (Xie and Fung, 2014; Wang and Hu, 2021). A number of comparative studies have ~~been carried out demonstrating~~ shown the superiority of non-local PBL schemes over local ~~ones at convective times where~~ schemes during convective periods when the uprising plume size is comparable to the vertical grid resolution (Arregocés et al., 2021; Banks et al., 2016; Hu et al., 2010; Xie et al., 2012; Xie and Fung, 2014). With ~~increasing affordability in~~ the growing affordability of increased CPU time, recent studies ~~deploying~~ using higher-order turbulence closure models have shown substantial improvements in wind ~~speeds and temperature in~~ speed and temperature predictions under complex atmospheric conditions compared ~~to the~~ with first-order ~~ones~~ schemes (Chen et al., 2022; Olson et al., 2019; Zonato et al., 2022).

The TKE-ACM2 PBL scheme (Zhang et al., 2024) is ~~one of the~~ a recently developed 1.5-order ~~schemes~~ scheme featuring a non-local transport component based on the transilient matrix approach adopted from Pleim (2007a, b). Zhang et al. (2024) ~~has shown~~ evaluated the model's performance by comparing it with measurements obtained by LiDAR units and surface stations, classified as urban or non-urban according to the landuse of the nearest model cell during preprocessing. They showed that the TKE-ACM2 ~~exhibits improvements in predicting the vertical profiles of wind speeds compared to~~ outperformed two other operational PBL schemes~~Boulac~~, Boulac (Bougeault and Lacarrere, 1989) and ACM2 (Pleim, 2007b)~~, however~~, in simulating the vertical profiles of wind speeds. However, overestimated wind speeds ~~persist in~~ persisted throughout the entire surface layer at ~~the urban station likely~~ stations classified as urban type, probably due to the discrepancy ~~caused by~~ resulting from the Bulk parameterization of surface layer fluxes. Therefore, ~~this paper aims at further improving the skills~~ the present paper aims to further improve the application of TKE-ACM2 in ~~the urbanized area through~~urbanized areas by:

1. formulating ~~the~~ a numerical method to couple the TKE-ACM2 PBL scheme with the multi-layer BEP model;
2. validating the coupled models in a simplified building layout scenario under different idealized initial and bottom boundary conditions by benchmarking against a finer-scale and building-resolving computational fluid dynamics model, ~~e.g.,~~ such as the large-eddy ~~simulations~~ simulation (LES) model; and

3. applying the coupled models ~~to~~ in real case simulations over ~~a densely built area~~densely built areas, such as the PRD region, where the land occupied by medium- to high-rise buildings ~~account~~ accounts for a great proportion ~~in~~ of the total urbanized area. Subsequently, the performance of TKE-ACM2 coupled with BEP ~~will be evaluated , with particular interest in the simulated~~ is evaluated in terms of the wind speeds using ~~the measurements from the~~ measurements from a network of high-resolution wind speed LiDAR units.

Section 2 ~~outlines the description of~~ describes the model development, the ~~introduction of the~~ LES tool used to validate TKE-ACM2+BEP ~~at~~ in an idealized urban morphology setup, ~~and the information about~~ the observational instrument, and the Local Climate Zones (LCZ) used for real case simulations. Section 3 ~~compares~~ evaluates the performance of ~~both~~ the TKE-ACM2 and Boulac PBL schemes coupled ~~to BEP~~ with BEP by comparing them with LES under ~~different~~ various idealized convective conditions over a simplified staggered ~~buildings layoutwith the Bulk methods being the references~~building layout, using Bulk methods as the reference. Section 4 presents the ~~sensitivity of wind speed profiles to UCM and the results of~~ effects of TKE-ACM2 with/without BEP on potential temperature (θ) and wind speed (U) profiles in real case simulations~~using~~ , highlighting the differences between TKE-ACM2 and Boulac~~PBL schemes over a month in the year 2022.~~ .

2 Methodology and materials

2.1 Numerical method ~~to couple~~ for coupling TKE-ACM2 and BEP

The formulation and validation of the TKE-ACM2 PBL scheme ~~are detailed in~~ were detailed by Zhang et al. (2024). The remarkable difference between TKE-ACM2 and its predecessor ACM2 (Pleim, 2007b) ~~lies in~~ is that TKE-ACM2 adopts ~~the~~ a 1.5-order turbulence closure model to calculate the eddy diffusivity/viscosity, rather than using prescribed profiles for different stabilities. Moreover, TKE-ACM2 differs from Boulac in ~~the way~~ that the non-local transport of both the momentum and scalars under convective conditions ~~are~~ is reflected using the transilient matrix approach in TKE-ACM2, whereas Boulac parameterizes the transport of momentum based on the local gradient only and uses the counter-gradient method for potential temperature transport, which is not energy ~~conservative~~conserving. Following Pleim (2007b), the governing equation balancing the tendency terms for zonal (u) or meridional (v) wind, potential temperature (θ), and water vapor mixing ratio (q) with the vertical gradients of fluxes is ~~written as,~~

$$\frac{\partial\zeta}{\partial t} = -\frac{\partial}{\partial z}\overline{w'\zeta'} \tag{1}$$

where $\zeta \in \{u,v,\theta,q\}$~~, and the~~ . The vertical turbulent fluxes ~~consisting of~~ comprising the local gradient transport and transilient non-local transport are parameterized as ~~,~~

$$\overline{w'\zeta'}_I = -K_{\underline{I}}\,\underline{\frac{S_I(\zeta_{i+1}-\zeta_i)}{V_i\Delta z_I}}\;{}_{\zeta,I}\,\frac{S_I(\zeta^n_{i+1}-\zeta^n_i)}{V_i\Delta z_I} + \mathrm{Mu}\,(h-z_I)\left(\zeta^n_{1}-\zeta^n_{i}\right) \tag{2}$$

where the subscripts i (I) denote variables located at half (full) sigma levels, ~~K~~ $K_\zeta = K_h$ is the eddy ~~viscosity/diffusivity~~ diffusivity for $\zeta \in \{\theta,q\}$ and $K_\zeta = K_m$ is the eddy viscosity for $\zeta \in \{u,v\}$, V and S are the volume and surface ~~fraction~~

fractions not occupied by buildings, Mu is the upward convective transport rate, and h is the boundary layer height. Adding the environmental forcing acting on multiple model levels, the discretized form of Eqn.1 ~~can then be written as ,~~ is written as

$$\frac{\zeta_i^{n+1}-\zeta_i^{n}}{\Delta t} = \underbrace{f_{\text{conv}}\,\text{Mu}\,\zeta_1^{n}}_{\text{upward convective transport}} \underbrace{-\,f_{\text{conv}}\,\text{Md}_i\zeta_i^{n} + f_{\text{conv}}\,\text{Md}_{i+1}\zeta_{i+1}^{n}\frac{\Delta z_{i+1}}{\Delta z_i}}_{\text{donward transport}} + \underbrace{(1-f_{\text{conv}})\frac{1}{V_i\Delta z_i}\left[S_I\frac{K_{\zeta,I}\left(\zeta_{i+1}^{n}-\zeta_i^{n}\right)}{\Delta z_I} - S_{I-1}\frac{K_{\zeta,I-1}\left(\zeta_i^{n}-\zeta_{i-1}^{n}\right)}{\Delta z_{I-1}}\right]}_{\text{local transport}} + \underbrace{\frac{F_i}{\Delta z_i}}_{\text{env. forcing}} \tag{3}$$

where the superscript $n+1$ ~~means~~ indicates the time forwarding by a ~~time-step~~ timestep (Δt), f_{conv} is the ratio that partitions the local and non-local transport, Md is the downward compensatory transport rate, and Δz is the vertical resolution. The original ~~formulation~~ formulations of f_{conv}, Mu, and Md ~~are detailed in~~ were detailed by Pleim (2007b), and the model sensitivity to some of these parameters ~~can be found in~~ was given by Zhang et al. (2024). The last term on the RHS of Eqn.3~~denoting the ,~~, denoting collective forcing from both the urban area and ~~natural~~ non-urban (natural) area for the first model layer ($i=1$), is computed using the weighted sum approach if the urban fraction (Urb) is less than 1~~,~~; i.e., $F_1 = (1-\text{Urb})F_{natural,1} + \text{Urb}F_{urban,1}$. For model layers $i>1$, the environmental forcing F_i is $\text{Urb}F_{urban,i}$ alone. Readers interested in the parameterization of F_{urban} are referred to the work of Martilli et al. (2002). Effectively, F_i is computed in the subroutine phys/module_sf_bep.F, resulting in the term $F_i/\Delta z_i$ being written as the combination of implicit (A_i) and explicit (B_i) parts~~,~~; i.e., $F_i/\Delta z_i = A_i\zeta_i + B_i$ for matrix inversion.

The prognostic equation ~~of~~ for TKE (e) in TKE-ACM2 coupled with BEP ~~remains identical to~~ is identical to that given by Zhang et al. (2024), but the parameterizations of each source/sink term are modified mainly to account for 1) the external TKE source converted from mean kinetic energy when flow separates ~~,~~ and 2) the altered characteristic length scale for eddies in the wake region due to buildings. According to Bougeault and Lacarrere (1989) and Makedonas et al. (2021), the prognostic equation ~~of~~ for e ~~by~~ considering the building effects ~~can be written as,~~ is

$$\frac{\partial e}{\partial t} = -\frac{1}{\rho}\frac{\partial}{\partial z}\rho\overline{w'e} - \overline{u'w'}\frac{\partial u}{\partial z} - \overline{v'w'}\frac{\partial v}{\partial z} + \beta\overline{w'\theta'} - \epsilon + \frac{\partial F}{\partial z} \tag{4}$$

where ρ is the density of air, β is the buoyancy coefficient, and $\epsilon = \rho C_\epsilon e^{3/2}/l_\epsilon$ represents the TKE dissipation rate ~~with C_ϵ and l_ϵ being~~ where $C_\epsilon = 1/1.4$ is an empirical constant and l_ϵ corresponds to the characteristic length of energy-containing eddies~~, respectively~~. The turbulent fluxes for momentum and heat are already given in Eqn.2. $\partial F/\partial z$ representing TKE generated by buildings can be written in a similar manner to momentum/heat as $Ae+B$ ~~which are~~ and is readily available from the BEP module in WRF. Assuming that the vertical turbulent transport of TKE mimics that of ~~the passive scalar~~passive scalars, the parameterization of $\overline{w'e}$ is expressed similarly to Eqn.2 ~~:~~ as

$$\overline{w'e}_I = -K_{e,I}\frac{S_I(e_{i+1}-e_i)}{V_i\Delta z_I} + \text{Mu}(h-z_I)(e_1-e_i) \tag{5}$$

The eddy diffusivity ~~for scalar~~ is equal in magnitude for scalars (K_h) and TKE (K_e) ~~are equal in magnitude and can be~~ and is related to eddy viscosity (K_m) ~~using~~ through the turbulent Prandtl number (Pr_t)~~:~~, which is a key parameter pertinent to heat transfer (Li, 2019):

$$K_e = K_h = K_m/\mathrm{Pr}_t \tag{6}$$

where $K_m = C_K l_k e^{1/2}$, C_K is a $\mathcal{O}(1)$ empirical constant, the parameterization of Pr_t is consistent with that presented by Zhang et al. (2024), which follows Businger et al. (1971), and the length scale l_k is modified from that calculated ~~in~~ by Bougeault and Lacarrere (1989) ($l_{k,\mathrm{old}}$) because the buildings ~~can~~ generate vortices whose size of $l_{\mathrm{build.}}$ is comparable to the building spatial dimension (typically the building height), according to Martilli et al. (2002)~~, as shown in Eqn.7. ,~~. This is expressed by

$$\frac{1}{l_k} = \frac{1}{l_{\mathrm{old}}} + \frac{1}{l_{\mathrm{build.}}} \tag{7}$$

~~Likewise, the~~ The same modification applies to l_ϵ, which ~~effectively indicates~~ suggests an enhanced dissipation of TKE (Martilli et al., 2002).

~~With the aforementioned parameterizations of intermediate parameters,~~ Ultimately, solving Eqn.3 ~~can be solved by writing into a linear system of $\mathbf{Ax} = \mathbf{b}$, where the column vector $\mathbf{x}$ contains the unknown prognostic variable ζ_i^{n+1}, the square boarded band matrix $\mathbf{A}$ is the coefficient matrix which consists of the first column entry ($\mathbf{E}$), diagonal ($\mathbf{D}$), upper diagonal ($\mathbf{U}$), and lower diagonal ($\mathbf{L}$) elements, and the column vector $\mathbf{b}$ is composed of the explicit terms in Eqn.3. To keep the same order of numerical accuracy as TKE-ACM2 (Zhang et al., 2024), the Crank-Nicolson scheme is retained which splits ζ_i^{n+1} to $C\zeta_i^{n+1} + (1-C)\zeta_i^n$ with $C = 0.5$ being the Crank-Nicolson factor. Subsequently, the $i-$th row and $i-$th column element of $\mathbf{D}$ can be expressed as,~~

$$\begin{aligned}\mathbf{D}_{i,i} &= 1 + C f_{\mathrm{conv}}\,\mathrm{Md}_i \Delta t \\ &+C\left(1-f_{\mathrm{conv}}\right)\frac{\Delta t}{\Delta z_i}\left(\frac{K_I S_I}{\Delta z_I}+\frac{K_{I-1}S_{I-1}}{\Delta z_{I-1}}\right) - CA_i\Delta t\end{aligned}$$

is straightforward using the computed K_ζ values derived from Eqn.6. The ~~$i-$th row element of column vector $\mathbf{b}$ is expressed as:~~

$$\begin{aligned}\mathbf{b}_i &= \zeta_i^n + (1-C) f_{\mathrm{conv}}\,\mathrm{Mu}\zeta_1^n \Delta t \\ &-(1-C) f_{\mathrm{conv}}\,\zeta_i^n \Delta t + (1-C) f_{\mathrm{conv}}\,\mathrm{Md}_{i+1}\zeta_I^n \frac{\Delta z_{i+1}}{\Delta z_i}\Delta t \\ &+\frac{1-C}{V_i \Delta z_i} f_{\mathrm{conv}}\,(K_I S_I \frac{\zeta_{i+1}^n - \zeta_i^n}{\Delta z_I} \\ &-K_{I-1}S_{I-1}\frac{\zeta_i^n - \zeta_{i-1}^n}{\Delta z_{I-1}})\Delta t + (1-C)A_i \zeta_i^n \Delta t + B_i \Delta t\end{aligned}$$

~~The $i-$th row and $j-$th column element of $\mathbf{U}$, $\mathbf{L}$, and $\mathbf{E}$, are the same to Eqn.13, Eqn.14, and Eqn.15 in Zhang et al. (2024), respectively, except an additional multiple of S_I/V_i applies to K_I~~ finite difference method used to obtain numerical solutions for Eqn.3 is described in detail in Appendix A.

2.2 Large-eddy simulation model

Prior to implementing the TKE-ACM2 PBL scheme coupled with BEP in real case simulations, we performed idealized simulations using prescribed surface heat fluxes along with simplified urban morphology~~and benchmarked it against one of the~~. We then benchmarked the results against those of PALM, a state-of-the-art ~~and building-aerodynamics-resolved large-eddy simulation (LES) models, i.e., the PALM model~~ LES model capable of resolving building aerodynamics. The PALM model (Maronga et al., 2015; Raasch and Schröter, 2001) is a non-hydrostatic incompressible Navier-Stokes equation solver ~~, which is~~ that has been rigorously evaluated against experiments~~and~~. It thus often serves as ~~the~~ a benchmark for deriving new parameterizations ~~regarding the~~ of boundary layer turbulent mixing ~~processes in the~~ in mesoscale weather forecasting ~~model. It utilizes~~ models. PALM uses a 1.5-order turbulence closure model for solving anisotropic turbulence in three dimensions simultaneously. One salient advantage of PALM ~~compared to~~ over other wall-resolved LES models is that PALM adopts ~~the~~ MOST between the solid boundary and the first model layer above, which greatly ~~elevates the~~ increases computational efficiency while preserving ~~the~~ accuracy in the context that the mesoscale model has $\Delta z \in \{\mathcal{O}(10)\,\mathrm{m}, \mathcal{O}(1000)\,\mathrm{m}\}$.

2.3 Idealized ~~simulations~~ simulation setup

A $1\,\mathrm{km}$ long by $1\,\mathrm{km}$ wide by $1.5\,\mathrm{km}$ high domain with equidistant spatial ~~resolution~~ resolutions $\Delta x = \Delta y = \Delta z = 5\,\mathrm{m}$ ~~with~~ and staggered building arrays ~~is~~ was set up for the PALM model. Fig.1 provides a plan view ~~for~~ of the domain setup and urban morphology configuration, where ~~the spatial dimension of the building follows a~~ buildings have a cross-section of $20\,\mathrm{m}$ square ~~cross-section with~~ and a height of $40\,\mathrm{m}$ and the windward wall ~~faces perpendicularly~~ is perpendicular to the upwind flow. The prescribed height of building arrays is justified by the fact that it is commonly seen in ~~the domain of interest (Hong Kong)(Kwok et al., 2020)~~Hong Kong according to Kwok et al. (2020). The street width in both horizontal directions is ~~chosen~~ set as $30\,\mathrm{m}$ to ~~mimic~~ align with a moderately densely built environment. ~~Such~~ The street width to building width ratio $(2/3)$ is deemed an "open" exposure in urban areas and has good representativity in Hong Kong. Unlike PALM~~runs at the building-resolved~~, which operates at a building-resolving scale, WRF+BEP ~~is at the~~ runs at a building-parameterized scale ($\Delta x = \Delta y = 1\,\mathrm{km}$), where explicitly resolving ~~the~~ building aerodynamics is impractical. ~~Therefore, we prescribe~~ We thus prescribed the urban morphological parameters to be consistent with PALM in the WRF+BEP look-up table required for BEP. The ~~horizontal extension of~~ WRF+BEP domain ~~is set as~~ was horizontally extended to $20\,\mathrm{km}$ by $20\,\mathrm{km}$ to ~~accommodate the thermal plumes of large scale~~ capture large-scale thermal plumes in the convective flow (Schmidt and Schumann, 1989)~~, while the same height of~~. The domain height remained $1.5\,\mathrm{km}$~~is retained but with slightly coarser~~, but with a slightly coarser vertical resolution of $\Delta z = 12.5\,\mathrm{m}$.

The initial condition ~~is prescribed as~~ was set $u_0 = u_g = 10\,\mathrm{m/s}$ ~~uniformly distributed~~ with a uniform distribution along the vertical direction and $v_0 = v_g = 0\,\mathrm{m/s}$, where u_g and v_g are ~~the~~ geostrophic winds with the Coriolis parameter being $10^{-4}\,\mathrm{s}^{-1}$. Two initial potential temperature profiles ~~are~~ were selected for the idealized simulations, one ~~being the~~ corresponding to a moderately convective atmosphere ($\overline{w'\theta'}_0 = 0.10\,\mathrm{K\,m^{-1}\,s^{-1}}$, denoted as Case 10WC) with no capping inversion and the other representing strongly convective atmospheric stability ($\overline{w'\theta'}_0 = 0.24\,\mathrm{K\,m^{-1}\,s^{-1}}$, denoted as Case 24SC) with a strong capping

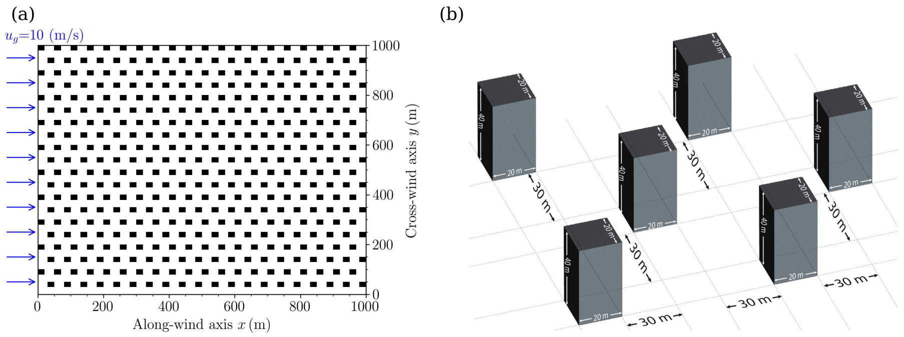

Figure 1. a) ~~The plan~~ Plan view ~~for~~ of domain setup; b) configuration of the urban morphology~~configuration~~.

inversion to limit the growth of the boundary layer. The analytical expressions of two initial θ profiles are ~~listed~~ given below, where $\partial\theta/\partial z$ in the free ~~atmospheres~~ atmosphere is $1\,\mathrm{K}/100\,\mathrm{m}$ in both cases~~,~~ :

$$\text{Case 10WC}: \quad \theta_0(z_i) = \begin{cases} 300\mathrm{K}, \quad z_i < 600\mathrm{m} \\ 300\mathrm{K} + 1/100(z_i - 600)\mathrm{K}, \quad z_i \geq 600\mathrm{m} \end{cases} \tag{8}$$

~~and~~

and

$$\text{Case 24SC}: \quad \theta_0(z_i) = \begin{cases} 300\,\mathrm{K}, \quad z_i < 600\,\mathrm{m} \\ 300\mathrm{K} + 6/100(z_i - 600), \quad 600\,\mathrm{m} \leq z_i < 800\,\mathrm{m} \\ 300\,\mathrm{K} + 6/100(800-600)\mathrm{K} + 1/100(z_i - 800)\,\mathrm{K}, \quad z_i \geq 800\mathrm{m} \end{cases} \tag{9}$$

All boundary conditions ~~are~~ were identically set in ~~both~~ the PALM and WRF+BEP simulations. The lateral boundary conditions for the along-wind direction (x) and cross-wind direction (y) ~~are~~ were set as periodic to simulate an infinitely long urban fetch. The bottom boundary conditions for heat ~~are~~ were reflected by different values of $\overline{w'\theta'}_0$ and a free-slip condition was set for the top boundary condition~~is free-slip~~. The microscale roughness length (z_0) was set as 0.01 m for both the ground and roof ~~is chosen as 0.01 m~~ in PALM, ensuring consistency with the value in the look-up table used ~~in~~ for WRF+BEP. The runtime parameters ~~that are crucial~~ needed to obtain meaningful results (Ayotte et al., 1996; Nazarian et al., 2020) for PALM and WRF+BEP are described in ~~a more detailed way~~ more detail in Section 3. The ~~temperature~~ temperatures of solid surfaces (~~roof, wall~~roofs, walls, and streets) in PALM and WRF+BEP are prescribed as 300 K.

2.4 ~~Local Climate Zones (LCZ)~~Real case simulation materials

~~Default 21-class MODIS or 24-class USGS landuse dataset may be obsolete or inaccurate in capturing the high heterogeneity of the urbanized surfaces in a particular domain. For instance, only 3 urban types are distinguished in the MODIS/USGS, resulting in a less resolved variability in urban morphological parameters in different urban landuse. In contrast, the~~

2.4.1 Landuse data and wind LiDAR observation network

This study adopted the 17-class LCZ classification scheme ~~provides a more detailed description of urban landuse at the local scale (10^{-2}~~ (Demuzere et al., 2022) to more accurately capture the highly variable urban morphology within the domain of interest. The distribution of LCZ 1 to ~~10^{-4} m). The superiority of LCZ classification over MODIS is proven~~ 10 (urban) grids and LCZ A to G (non-urban) grids is depicted in Fig.2c. Each class is defined in Table B1.

A wind speed Doppler LiDAR network (see Fig.2d) has been operational in Hong Kong ~~region revealed by Du et al. (2023). Each urban type represents a distinct urban morphology configuration, and LCZ class 1 to 10 covers from the most compactly built to the sparsely built environment, which can greatly aid the investigation of meteorological variables in a highly heterogeneous domain. In this study, we adopted the recently updated and well-validated LCZ global map developed by Demuzere et al. (2022) to characterize the urban surfaces in the innermost nested domain (D4), shown in Fig.2b. The distribution of 17 classes is plotted in logarithmic y scale in Fig.2c. What should be highlighted from the LCZ map is that the proportion of compact high-rise type (~~since March 2020, continuously monitoring wind conditions and playing a crucial role in validating regional downscaling results. The network comprises three WindCube 100S LiDAR units manufactured by Vaisala. Each unit measures the vertical profile of the wind speed at an elevation angle of 90°. The units measure 25-m intervals starting from 50 m above ground level, with an accuracy of $< 0.5\,\mathrm{m/s}$ for wind speed and 2° for wind direction. Although each LiDAR outputs data at a frequency of 1 Hz, measurements are averaged hourly and archived due to storage limitations. We represent the land cover type of each LiDAR unit using the LCZ classification associated with the nearest model grid following Ribeiro et al. (2021).

The LiDAR unit at the Hong Kong University of Science and Technology Supersite (USTSS_LCZ5) is located on the east coast of Kowloon Island, where the nearest model grid center falls within LCZ 5 (open mid-rise). The second LiDAR, installed on the southeastern peninsula of Hong Kong Island (Hok Tsui), is surrounded by natural vegetation and referred to as HT_rural. Lastly, the LiDAR at King's Park in downtown Kowloon, where the average building height is 60 m (Kwok et al., 2020), is located within an LCZ 1 ~~) and open high-rise type (LCZ 2)is considerably higher compared to European cities focusing on a similar scale, e.g.~~ model grid (compact high-rise), ~~Vienna (Hammerberg et al., 2018), Barcelona (Ribeiro et al., 2021), reinforcing the demand of a multi-layer building effects parameterization coupled to the PBL scheme~~and designated as KP_LCZ1.

In addition to profiler-type observations, we also used measurements of surface meteorological variables, including the 10-m wind speed (U_{10}), 2-m temperature (T_2), and 2-m relative humidity (RH_2), retrieved from the Global Telecommunication System. The coordinates and LCZ classifications of these surface stations are provided in the supplementary material of Zhang (2024). The surface station dataset comprises a total of 13 urban stations characterized by LCZ classes 1 to 10, along with 10 stations situated on water surfaces, and 8 rural stations on land. The distribution of surface stations across specific LCZ classes is provided in Table B1.

2.5 ~~Real case simulations setup~~

2.4.1 Configuration of real case simulations

A four-nested domain ~~adopting the~~ having a parent domain grid ratio of 1:3 ~~with~~ and a reference latitude of 28.5 °N and ~~a~~ longitude of 114 °E (Fig.2a) ~~is chosen~~was adopted. The coarsest domain (D1) with $\Delta x = \Delta y = 27\,\mathrm{km}$ ~~spans~~ spanned 283 grid points in the East-West direction and 184 grid points in the North-South direction, covering the ~~entire~~ entirety of China. The finest domain (D4), with a horizontal resolution of $1\,\mathrm{km}$~~focuses~~ , focused on the PRD region, ~~where there exist a few~~ which encompasses heavily populated and densely built mega-cities including Hong Kong (7.3 million people as of 2021), Shenzhen (17.6 million), and Guangzhou (18.7 ~~), with the number in the brackets showing the population in the unit of millionas of the year 2021.~~ million). The surface stations and high-resolution wind speed LiDAR locations deployed in D4 are highlighted in Fig.2d. 30-day simulations ~~are performed between July 18 20 o'clock local time (LT) to August 18 20LT in~~ were performed from 1200 UTC+0 on 18th July to 1200 UTC+0 on 18th August of year 2022. The integration ~~is performed by overlapping one day as~~ was performed using a one-day overlap for the spin-up between two consecutive four-day segments.

~~We configured~~ The configuration of real case simulations is outlined in Table B2. We configured the WRF eta levels such that multiple vertical model grids ~~can intersect~~ intersected the UCL and RSL. Thus, the variability of wind speeds ~~can be~~ was better represented by BEP ~~in the presence of buildings~~ where buildings were taller than the first above-ground full eta level. The lowest ~~6~~ six half eta levels ~~correspond~~ corresponded to approximately $9\,\mathrm{m}$, $28\,\mathrm{m}$, $49\,\mathrm{m}$, $71\,\mathrm{m}$, $96\,\mathrm{m}$, and $122\,\mathrm{m}$ above ground level (AGL). We used NCEP GFS analysis data at 6-hourly input intervals to provide the initial and lateral boundary conditions. ~~Noah~~

Identical physics schemes were chosen in the four simulations: the unified Noah scheme (Chen and Dudhia, 2001) for the land-surface model~~and revised MM5 surface layer scheme have been selected. Four simulations were performed using different PBL schemes and UCM . Namely, they are~~ , WSM 3-class simple ice scheme (Hong et al., 2004) for microphysics, RRTMG scheme (Iacono et al., 2008) for longwave/shortwave radiation, and Grell-Freitas ensemble scheme (Gall et al., 2013) for cumulus. The TKE-ACM2 PBL scheme was coupled with the BEP UCM (referred to as TKE-ACM2+~~Bulk,~~ BEP) and evaluated alongside the TKE-ACM2 scheme in isolation (TKE-ACM2+~~BEP, Boulac+Bulk, and~~ Bulk), where the surface layer fluxes were computed using the Noah land-surface model. The Boulac PBL scheme underwent the same evaluation, being coupled with the BEP UCM (Boulac+BEP~~. Other relevant setup in the namelist is detailed in Table A1. Meanwhile, the~~) and assessed in isolation with the Noah land surface model (Boulac+Bulk). The look-up table for LCZ class properties ~~which provides crucial parametersincluding~~ that provided crucial parameters, including the impervious fraction and building height distribution~~is also attached~~ , is included in the supplementary material of Zhang (2024).

3 Idealized simulations results

Nazarian et al. (2020) ~~show~~ showed the importance of choosing appropriate runtime parameters for LES in a neutral atmosphere over building arrays. ~~Since this study adopts~~ As the present study adopted two convective scenarios in a similar urbanized

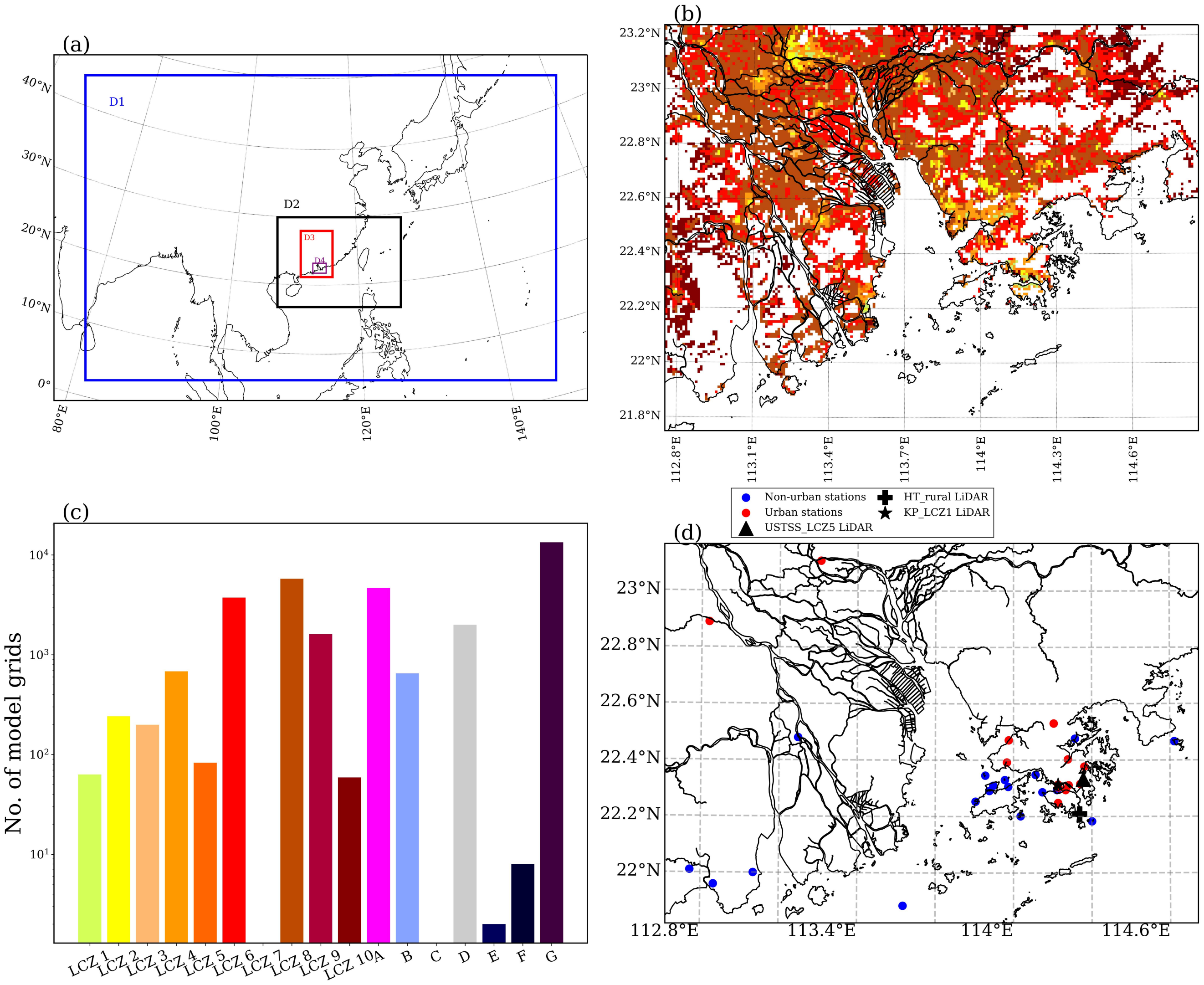

Figure 2. a) ~~The four-nested~~ Four-nested domain; b) LCZ ~~classification~~ urban grids (LCZ 1 to 10) for ~~1-km resolution~~ domain 4 having 1-km resolution with the color scheme represented in panel c); c) ~~LCZs~~ LCZ distribution in D4; d) ~~Distribution~~ distributions of surface stations and wind speed LiDAR.

domain, extra attention ~~must~~ needs to be paid to ~~the~~ thermal characteristics in determining the runtime parameters. As revealed by Ayotte et al. (1996) and Shin and Dudhia (2016), the ~~duration~~ durations of simulations can be determined by examining the temporal variation of turbulence statistics. We first examined the time required for LES to reach a quasi-equilibrium state by investigating the variation of the maximum resolved TKE ($e_{\mathrm{res.}}$) and the absolute value of the maximum vertical velocity ($|w_{\max}|$), shown in Fig.3.

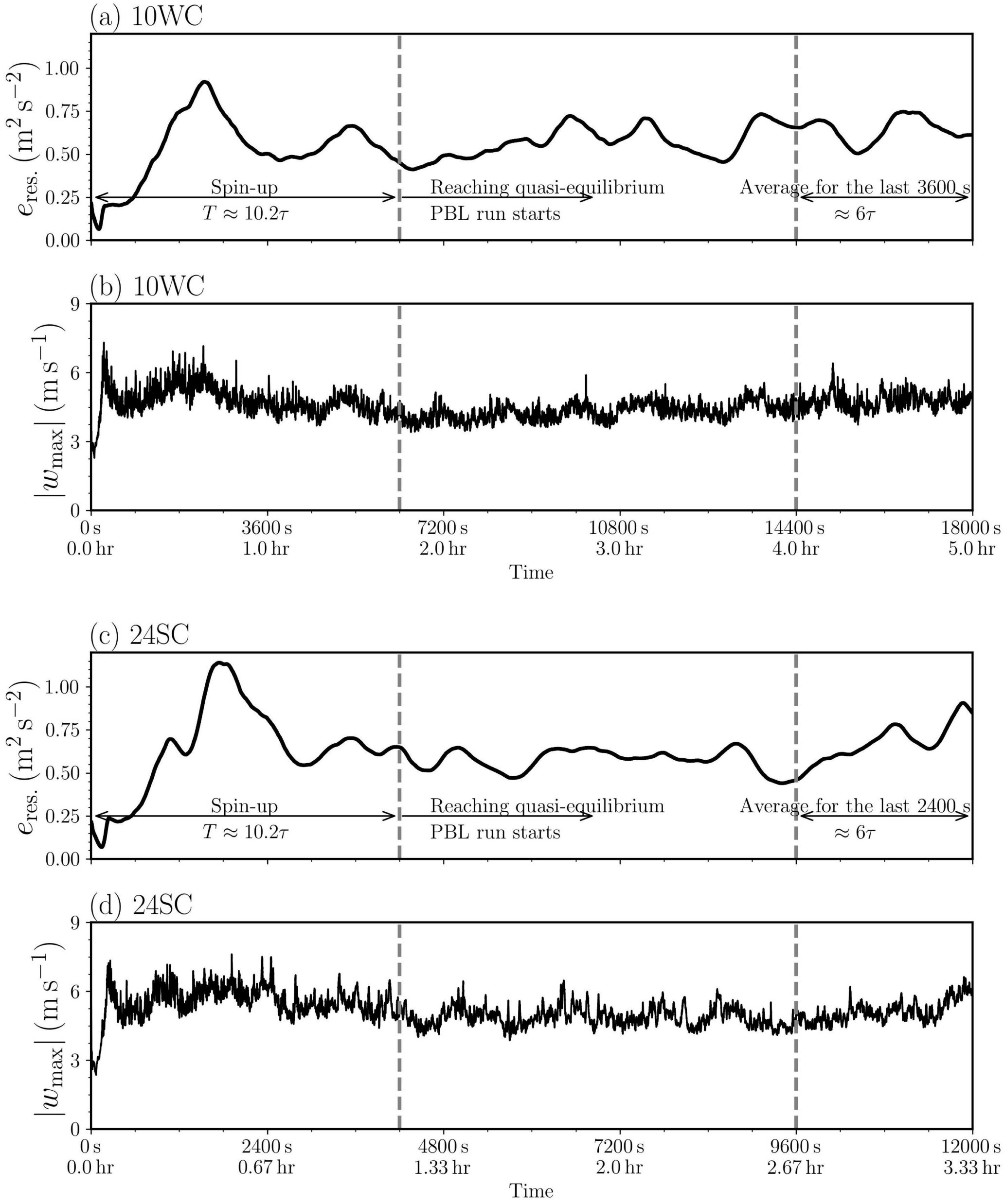

Figure 3. a) ~~The time~~ Time series of $e_{\text{res.}}$ for Case 10WC; b) ~~The~~ time series of $|w_{\text{max}}|$ for Case 10WC; c) ~~Same to~~ same as a) but for Case 24SC; d) ~~Same to~~ same as b) but for Case 24SC.

~~It is found the quasi-equilibrium is reached in both cases when LES runs for~~ Quasi-equilibrium was achieved in the two LES cases after approximately 10.2 convective turnover times (τ), where $\tau = h/w^*$ ~~is the convective time scale~~ , and $w^* =$

$(\beta\overline{w'\theta'}_0 h)^{1/3}$ ~~is~~ represents the convective velocity scale. The duration of 10.2 large-eddy turnover ~~time is deemed~~ times was considered a reasonable indicator ~~for~~ of well-developed dynamic fields over the domain with buildings~~compared to other studies adopting a factor~~, especially compared with other studies that have used factors of 5 (Ayotte et al., 1996; Pleim, 2007b; Zhang et al., 2024) and 6 (Shin and Dudhia, 2016) ~~over a flat domain. The u,θ fields are horizontally averaged~~ for flat domains.

The horizontal averages of the velocity and potential temperature fields were calculated at 10.2τ and ~~used~~ served as initial conditions ~~to drive WRF +BEP simulations for another~~ for driving mesoscale WRF simulations for an additional 20τ. Subsequently, the results ~~during the last~~ from the final 6τ~~corresponding to 3600 s or 2400 s are~~, corresponding to either 3600 seconds or 2400 seconds, were averaged both horizontally and temporally~~averaged for comparison. The 6τ averaging interval is consistent with Ayotte et al. (1996); Pleim (2007b); Zhang et al. (2024)~~. Table 1 summarizes the key turbulence characteristics of the convective flow and the runtime parameters.

Table 1. Turbulence characteristics and runtime parameters

Parameter	Case 10WC	Case 24SC
Capping inversion strength	N.A.	$\frac{\partial\theta}{\partial z} = 6/100,\ \mathrm{K/m}$
PBL height, $h(t = 10.2\tau)$	$840\,\mathrm{m}$	$720\,\mathrm{m}$
Large-eddy turnover time, τ	$600\,\mathrm{s}$	$404\,\mathrm{s}$
Convective velocity scale, w^*	$1.40\,\mathrm{m/s}$	$1.78\,\mathrm{m/s}$
Spin-up time (10.2τ)	$6{,}300\,\mathrm{s}$	$4{,}200\,\mathrm{s}$
Duration of simulation (30τ)	$18{,}000\,\mathrm{s}$	$12{,}000\,\mathrm{s}$
Averaging time (last 6τ)	$3{,}600\,\mathrm{s}$	$2{,}400\,\mathrm{s}$

The horizontally averaged ~~u,θ~~ u and θ profiles during the last 6τ are displayed in Fig.4 ~~. Meanwhile, the turbulence fluxes outputted~~ and the turbulent fluxes from PALM and computed from WRF PBL schemes are ~~plotted~~ contrasted in Fig.5. The total turbulent momentum flux in Boulac ~~is~~ was simply computed using the local gradient as -$K_m\partial u/\partial z$ ~~while~~ whereas the turbulent heat flux ~~needs to add~~ required the addition of the counter-gradient flux shown as $-K_h(\partial\theta/\partial z-\gamma)$.The root-mean-square-error (RMSE) for first-order moments u,θ and second-order moments $\overline{w'\theta'}$,$\overline{w'u'}$ calculated below the PBL height is displayed in Fig.6.

In Case 10WC~~where there is~~, with a moderate surface heat flux, both TKE-ACM2+BEP and Boulac+BEP ~~can reproduce~~ reproduced the unstable atmosphere below the inertial sub-layer (ISL)~~which is~~, which was located at approximately $3H$ (Fig.4a). However, Boulac+BEP ~~predicts~~ simulated a warmer bias in θ at the first model layer and a colder bias at ~~the~~ roof level, resulting in an excessively unstable UCL. In addition, the cold bias ~~persists in the entire~~ persisted throughout the mixed layer. ~~On the contrary~~In contrast, TKE-ACM2+BEP ~~produces a less~~ produced a smaller warm bias in the UCL. Furthermore, θ in the overlaying ISL ~~is~~ was well reproduced by TKE-ACM2+BEP. A deeper well-mixed boundary layer ($\partial\theta/\partial z \approx 0$) ~~can be simulated by~~ was simulated using TKE-ACM2+BEP, ~~while discrepancy from LES results is discovered in~~ and a discrepancy

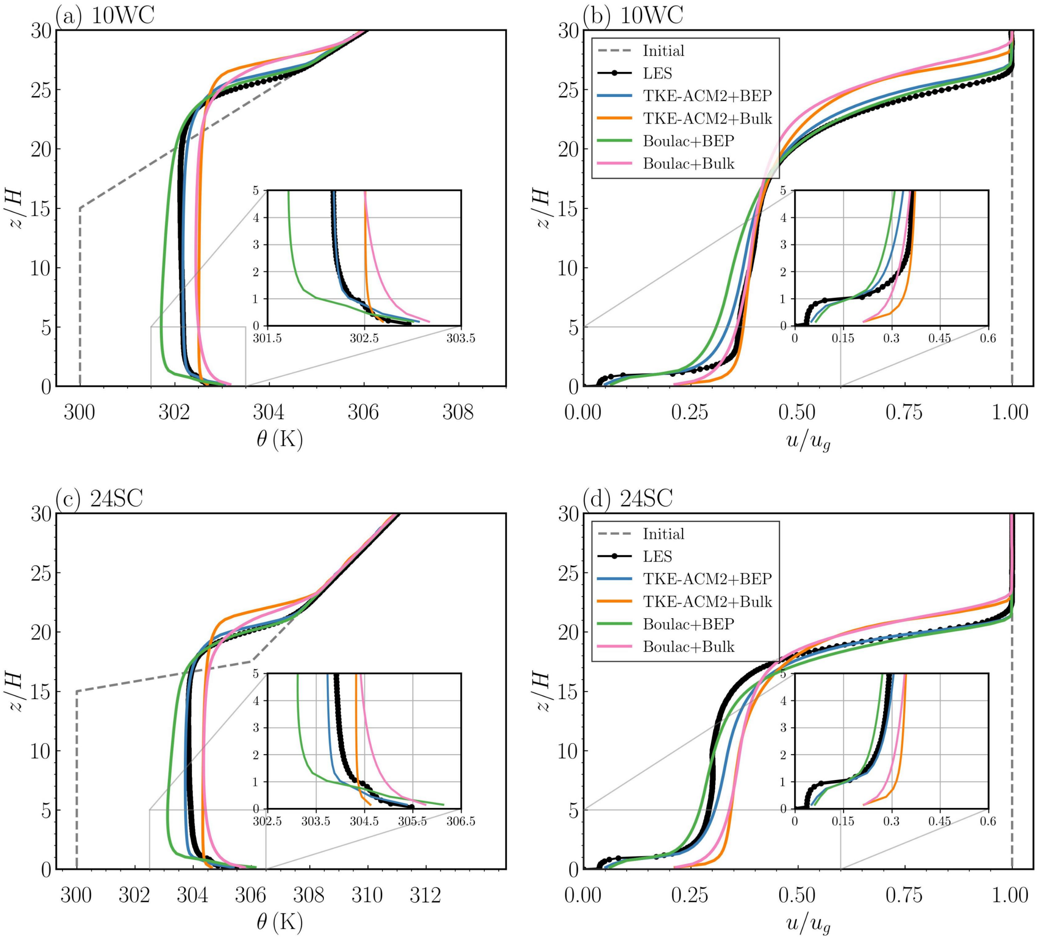

Figure 4. a) Horizontally averaged θ profile during the last 6τ for Case 10WC; b) ~~Horizontally~~ horizontally averaged u profile normalized by $u_g = 10\,\mathrm{m/s}$ during the last 6τ for Case 10WC; c) ~~Same to~~ same as a) but for Case 24SC; d) ~~Same to~~ same as b) but for Case 24SC. The ~~grey~~ gray dashed lines represent the initial conditions. The black ~~dots denote~~ dotted line shows the LES results. The solid blue, orange, green, and pink lines represent the results for TKE-ACM2+BEP, TKE-ACM2+Bulk, Boulac+BEP, and Boulac+Bulk, respectively.

in the Boulac+BEP ~~which suggests~~ results relative to the LES results suggests that the boundary layer ~~becomes~~ became stable from approximately $10H$. ~~In comparison~~ Relative to BEP simulations, the Bulk methods produce consistently overestimated θ within the PBL. ~~Inspecting the~~ Figure 4b suggests that the inflection point in the wind speed profile was well simulated at roof level in BEP and PALM, in contrast with the Bulk simulations, in which the wind shear ($\partial u/\partial z$) was relatively gentle at roof level. The momentum simulated by TKE-ACM2+BEP generally exhibited better agreement with observations than Boulac+BEP, especially within the mixed layer. The most visible negative bias of u in BEP simulations occurred at $[1H, 5H]$. It should be highlighted in Fig.4b that from the ground level to the top of the UCL, both BEP simulations overestimated the

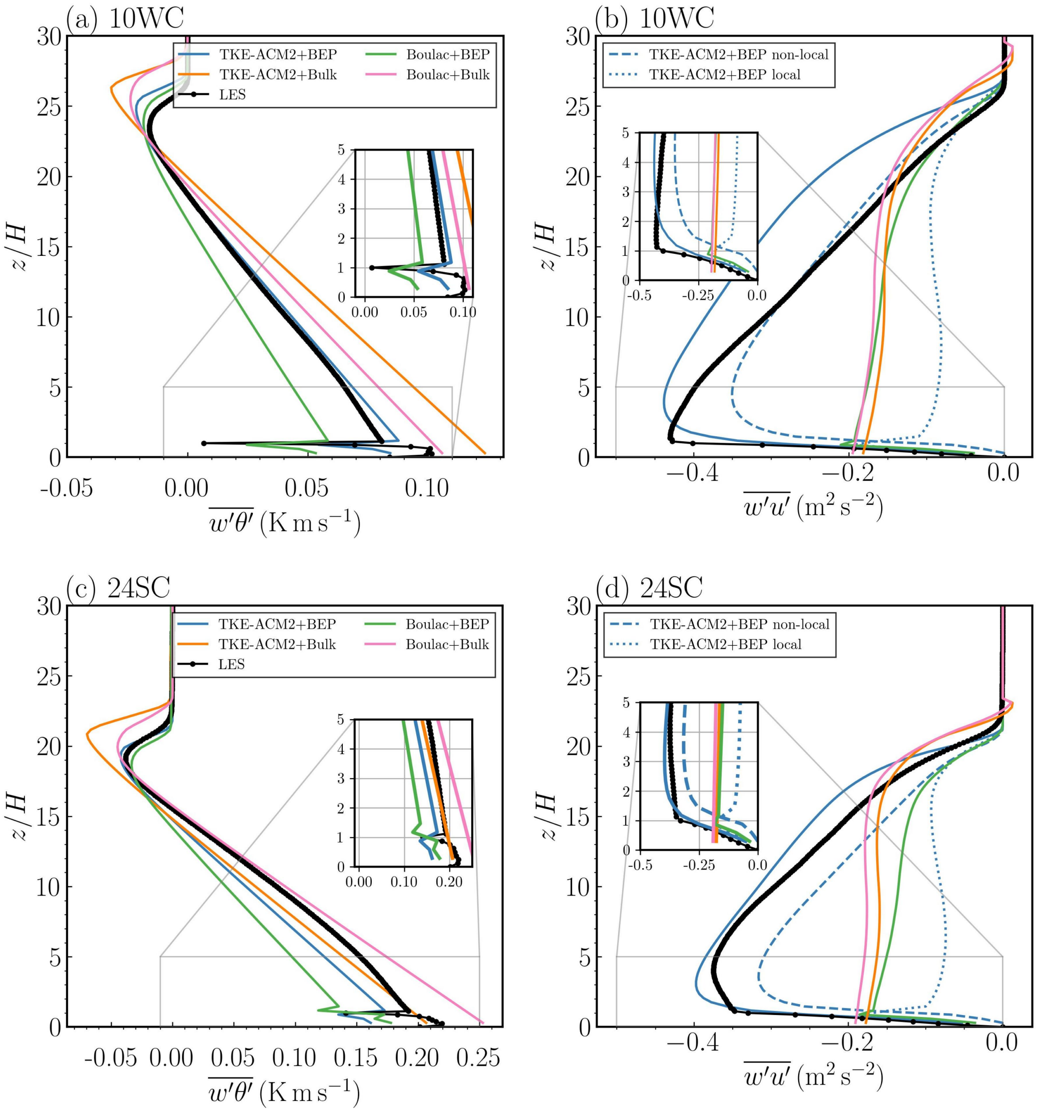

Figure 5. a) Horizontally averaged $\overline{w'\theta'}$ profile during the last 6τ for Case 10WC; b) ~~Horizontally~~ horizontally averaged $\overline{w'u'}$ profile during the last 6τ for Case 10WC; c) ~~Same to~~ same as a) but for Case 24SC; d) ~~Same to~~ same as b) but for Case 24SC. The black ~~dots denote~~ dotted line shows the LES results. The solid blue, orange, green, and pink lines represent results for TKE-ACM2+BEP, TKE-ACM2+Bulk, Boulac+BEP, and Boulac+Bulk, respectively. The blue dashed and blue dotted lines represent the ~~local and~~ non-local and local turbulent momentum fluxes of TKE-ACM2+BEP, respectively. The ~~profiles are zoomed in aside for $z/H \leq 5$. All $y-$axes are normalized by the uniform building height $H = 40\,\mathrm{m}$. The profiles are zoomed in aside~~ insets show magnified results for $z/H \leq 5$. All $y-$axes are normalized by the uniform building height $H = 40\,\mathrm{m}$.

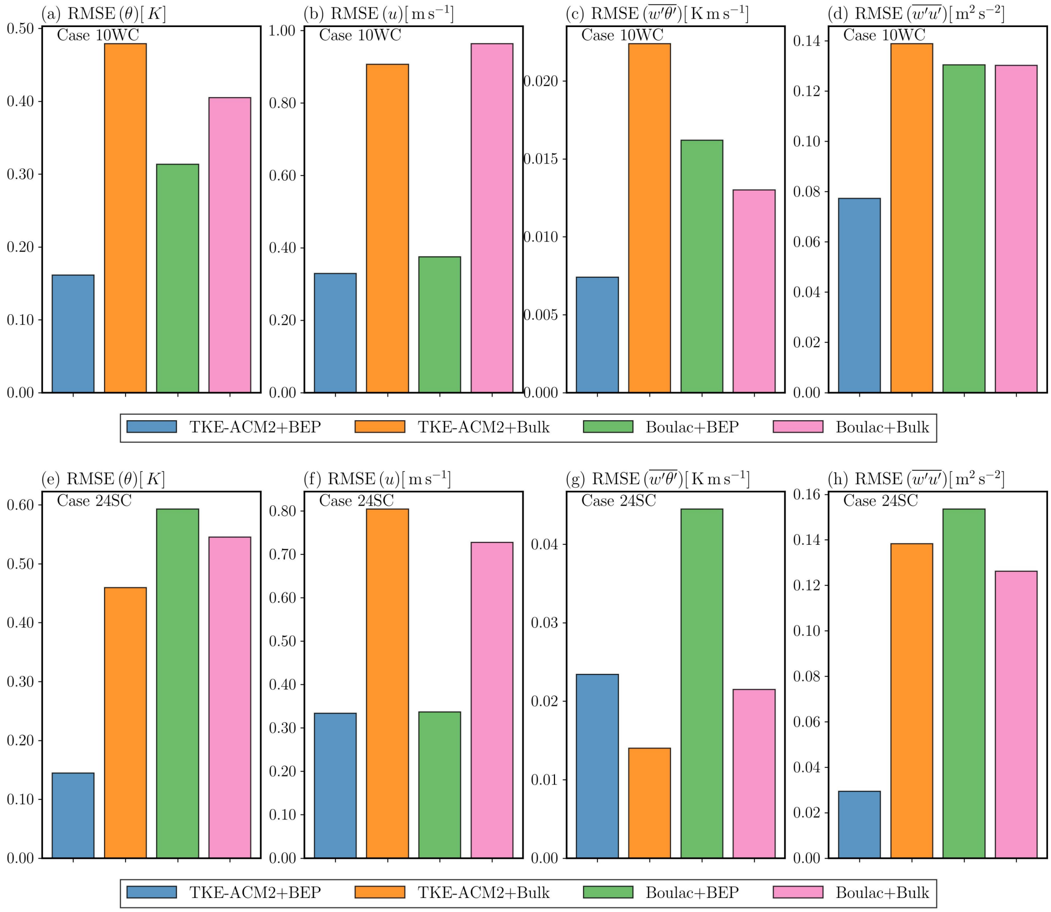

Figure 6. a-d): ~~RMSE~~ RMSEs for ~~$\overline{w'\theta'}$~~ θ, ~~$\overline{w'u'}$~~ u, ~~θ~~ $\overline{w'\theta'}$, and ~~u~~ $\overline{w'u'}$, calculated below the PBL height for Case 10WC by taking the LES results as the ground truth, respectively; e-h): ~~Same~~ same as a-d) but for Case 24SC.

wind speed in contrast with an underestimation in the mixed layer. It thus appears that the BEP parameterization resulted in an underestimation of wind shear at roof level when compared with the LES. The Bulk simulations clearly indicate that the lack of multi-layer parameterization of aerodynamic drag led to overestimation of the wind speed within the UCL.

The heat flux profile in Fig.5a reveals that the trends of variation ~~are~~ were well captured in the two BEP simulations~~where the sink of heat flux is reproduced~~ , in that the drastic reduction in heat flux when approaching the roof level from the ground ~~. This is attributed~~ was reproduced. This reduction is attributable to the prescribed temperature of the building wall and roof (300 K) being cooler than the atmosphere, leading to conduction. A possible explanation for the warm bias observed in both Bulk simulations is the lack of ~~heat sink~~ conduction between solid surfaces and the atmosphere beyond the first model layer. In general, TKE-ACM2+BEP ~~simulates~~ simulated a better matched $\overline{w'\theta'}$ profile in the mixed layer~~.~~, as shown in Fig.5a. In contrast, Boulac+BEP ~~produces~~ produced a $\overline{w'\theta'}$ vertical profile ~~of~~ with a weaker magnitude, which may account for the θ

profile becoming stable from $10H$. ~~However, greater discrepancies are~~ Greater discrepancies in the magnitude of $\overline{w'\theta'}$ were observed in TKE-ACM2+BEP within the UCL and near ~~PBL height~~ the PBL height, where the relatively constant $\overline{w'\theta'}$ in the ~~middle UCL is not exhibited~~ mid-UCL was not reproduced in either BEP simulation~~. The inflection point in the wind speed profile is well simulated at the roof level in BEP and PALM, opposite to Bulk simulations where the wind shear ($\partial u/\partial z$) is relatively gentle at the roof level . The momentum simulated by TKE-ACM2+BEP generally provides a better reproduction than Boulac+BEP, particularly in the mixed layer. The most visible negative bias of u in BEP simulations occurs at $1H, 5H$. It should be highlighted that from the ground level up to the top of UCL, both BEP simulations result in an overestimated wind speed as opposed to an underestimation in the mixed layer. This has shown the wind shear at the roof level is underestimated if the buildings are parameterized following BEP in contrast to that they are explicitly resolved. The Bulk simulations clearly indicate the lack of multi-layer parameterization of aerodynamic drag leads to significantly overestimated wind speed within the UCL. It is discovered that the momentum flux increases~~; however, the drastic reduction in $\overline{w'\theta'}$ at roof level was well captured, indicating that the physical interaction with buildings was reasonably considered. The momentum flux decreased from zero at the ground level to a maximum value at ~~some height~~approximately 2 to 4 times the canopy height, followed by a descending trend in BEP simulations, in contrast to the monotonically descending trend in simulations ~~where~~ when the Bulk method ~~is adopted~~was adopted, as shown in Fig.5a. However, Fig.5b suggests that the magnitude of $\overline{w'u'}$ simulated by the two schemes ~~exhibit~~ had greater discrepancies than that of $\overline{w'\theta'}$. Boulac+BEP ~~produces~~ consistently underestimated $\overline{w'u'}$. TKE-ACM2+BEP ~~results in~~ provided a slightly less biased $\overline{w'u'}$ but the maximum value ~~occurs~~ was at approximately $z/H = 4$, whereas LES ~~suggests~~ suggested the height at which $\overline{w'u'}$ ~~peaks~~peaked, $z/H_{\overline{w'u'}_{\max}}$, ~~is~~ was 1 in this case. The closer ~~match~~ alignment of $\overline{w'u'}$ simulated by TKE-ACM2+BEP is ~~attributed to the~~ attributable to the considerable contribution of non-local momentum flux~~contributing to a considerable prorportion~~. In summary, TKE-ACM2+BEP ~~is~~ was able to simulate a well-mixed boundary layer under such ~~a~~ prescribed convective atmospheric stability. The inflection point at ~~the roof level can be reproduced similarly~~ roof level could be reproduced in a manner similar to how Boulac+BEP behaves. In addition, TKE-ACM2+BEP ~~exhibits better ability in predicting~~ was better at simulating the θ and u ~~profile which is reflected in~~ profiles, as reflected by the ∼48.5% reduction ~~of~~ in RMSE(θ) and ∼12.2% reduction in RMSE(u) ~~compared~~ relative to Boulac+BEP.

~~Similar behaviors of the two schemes are found~~ Two PBL schemes performed similarly in Case 24SC, where TKE-ACM2+BEP ~~simulates a~~ simulated notably less warm bias in the UCL ~~, particularly at~~ shown in Fig.4c, particularly in the first model layer. ~~Additionally~~In addition, the θ profile extending from the UCL up to $18H$ ~~is~~ was considerably better reproduced by TKE-ACM2+BEP whereas Boulac+BEP ~~predicts~~ simulated consistently cold bias below the inversion. ~~This can be likely attributed to the more underestimated $\overline{w'\theta'}$ in the mixed layer simulated by Boulac+BEP (Fig.5c). The two Bulk simulations persist the warm bias throughout the PBL as in Case 10WC. A few similarities have been found~~ There were similarities in the momentum profile between the 24SC and 10WC cases. ~~Firstly,~~ First, Fig.4d shows that Boulac+BEP ~~predicts~~ predicted consistently lower wind speed than TKE-ACM2+BEP. ~~Secondly~~Second, both BEP simulations ~~tend to yield overestimated~~ tended to overestimate the wind speed in the UCL. ~~Thirdly~~Third, Bulk methods ~~cannot~~ did not reproduce the inflection point and ~~exhibit~~ exhibited the greatest positive bias in the UCL. ~~Lastly~~Finally, the wind shear at ~~the roof level displays~~ roof level had lower magnitudes in the two BEP simulations ~~compared to~~ than in LES. The difference in performance ~~is~~ was that TKE-

ACM2+BEP ~~exhibits~~ had slightly less deviation from $1H$ to approximately $5H$ ~~, but starts to visibly overpredict~~ but made obvious overpredictions in $[7H, 17H]$. In contrast, Boulac+BEP ~~shows~~ had a negative bias in $[1H, 7H]$ and ~~provides~~ provided a promising match in $[7H, 17H]$.

The heat flux profile for Case 24SC presented in Fig.5c shows a visibly underestimated $\overline{w'\theta'}$ in the mixed layer simulated by Boulac+BEP, which accounts for the cold bias. Conversely, the two Bulk simulations consistently had warm bias throughout the PBL, consistent with the trend in Case 10WC. Fig.5d indicates that TKE-ACM2+BEP ~~can generate~~ yielded $\overline{w'u'}$ ~~of~~ with a similar pattern and magnitude to LES in the whole PBL, whereas Boulac+BEP ~~seems~~ seemed to largely underestimate the momentum flux as observed in the 10WC case. ~~A~~ There was a notable difference in $z/H_{\overline{w'u'}_{\max}}$ ~~is found~~ between 24SC and 10WC~~: LES shows~~; i.e., LES showed that $z/H_{\overline{w'u'}_{\max}}$ ~~increases~~ increased from $z/H = 1$ to approximately $z/H = 4$ when ~~$\overline{w'u'}$ is~~ $\overline{w'\theta'}_0$ was stronger. Further analysis ~~by partitioning the~~ involving the partitioning of total $\overline{w'u'}$ ~~reveals~~ revealed that the non-local component ~~plays~~ played a more important role in distributing the surface layer fluxes to the mixed layer in TKE-ACM2+BEP, as reflected by the ~~red~~ blue dashed line in Fig.5d. Compared with Case 10WC, the larger prescribed $\overline{w'\theta'}_0$ in Case 24SC ~~suggests~~ suggested that TKE-ACM2+BEP ~~provides~~ achieved a closer match in the magnitude and shape ~~heat flux profile compared to~~ of $\overline{w'u'}$ at and immediately above roof level compared with Boulac+BEP~~when $\overline{w'u'}_0$ increases. Also~~. In addition, TKE-ACM2+BEP ~~reports~~ gave $z/H_{\overline{w'u'}_{\max}} = 3$, which ~~deviates less~~ aligns more closely with LES results than Boulac+BEP ($z/H_{\overline{w'u'}_{\max}} = 1$)~~, compared to LES results. Rotach (2001) investigated~~. Rotach (2001) analyzed several field measurements and wind tunnel experiments to examine the height of the maximum turbulence momentum flux. ~~Their results show~~ They found that $\overline{w'u'}$ can occur at approximately $3H$, which is deemed as the top of the ~~ISL~~RSL. This indicates that stronger heat flux can cause elevated $z/H_{\overline{w'u'}_{\max}}$, requiring extra caution in the PBL scheme when dealing with a sizable urban morphology. ~~Conclusively, TKE-ACM2+BEP outperforms Boulac+BEP in Case 24SC in simulating the θ profile by reducing RMSE by 75.6%, which is consistent with the closer match of $\overline{w'u'}$ in the mixed layer. The~~ In summary, the RMSE(u) ~~is fount to be both~~ was $0.33\,\mathrm{m\,s^{-1}}$ ~~in~~ for both TKE-ACM2+BEP and Boulac+BEP. ~~As a result, the performance of~~ This indicates that the two PBL schemes coupled with BEP ~~in predicting the momentum profiles is comparable statistically~~ performed similarly in simulating momentum profiles below the PBL height ~~and exhibits considerable superiority over~~ in Case 24SC and outperformed the Bulk methods. However, TKE-ACM2+BEP outperformed Boulac+BEP in Case 24SC in simulating the θ profile, reducing the RMSE by 75.6%, which aligns with its closer match of $\overline{w'\theta'}$ in the mixed layer.

4 Real case ~~simulations~~ simulation results

4.1 ~~Effects~~ Impact of ~~BEP~~ TKE-ACM2 on ~~U and~~ the vertical profiles of θ ~~over different LCZ types~~and U

~~Fig.A1 and Fig.A2 display~~ Figures C1 and C2 present the vertical profiles of θ and $U = \sqrt{u^2+v^2}$ averaged ~~in~~ over the entire simulated month ~~over LCZ classes 1-10~~for ten LCZ urban classes, water surfaces, and ~~other natural landuse. What should be highlighted from Fig.A1 and Fig. A2 is that TKE-ACM2+BEP produces larger U and warmer~~ rural land covers. Implementing the BEP scheme with both PBL schemes reduced θ ~~within the PBL height compared to Boulac+BEP over all~~ and U by up to approximately $2\,\mathrm{K}$ and $2\,\mathrm{m/s}$ respectively, below 35 times the maximum building height for each LCZ urban class ($H_{\max}$), with the most pronounced differences occurring near the ground. Both BEP simulations had less pronounced differences in U over water surfaces and rural land cover compared with urban grids, ~~corroborating the findings in Section 3. The differences in vertical profiles of~~ primarily because the BEP model was not directly applied in these non-urban areas. Any observed differences in U in these regions resulted from the neighboring urban grids. The effects of BEP on U over urban grids align with simulations conducted for Berlin, Munich, and Prague (Karlický et al., 2018). Finally, complex interactions between the atmosphere and buildings, including radiative transfer (direct and reflected solar radiation and net longwave radiation), and thermal exchange between solid surfaces and the atmosphere, collectively led to the lower temperature in BEP simulations.

The influence of the TKE-ACM2 PBL scheme was assessed by comparing θ and U profiles with those from Boulac, both with and without BEP, as shown in Figs.7 and 8. TKE-ACM2 generally predicted a warmer θ ~~between the BEP and Bulk methods are shown in Fig. 7 and Fig. 8 with the shadowed area representing ± 1 standard deviation (σ)over the whole month~~than Boulac across urban, water, and rural grids, regardless of BEP activation. However, the difference $\Delta\theta(\mathrm{TKE\text{-}ACM2} - \mathrm{Boulac})$, was slightly less in the BEP simulations than in Bulk simulations across all grids.

Moreover, TKE-ACM2 consistently simulated higher wind speeds above the canopy height than Boulac, particularly when paired with BEP, aligning with results from idealized simulations (Figs.4b & 4d). There were instances where the average $\Delta U(\mathrm{TKE\text{-}ACM2} - \mathrm{Boulac})$ was negative at the first model height (9 to 10 meters) for the Bulk method, notably at LCZ 1, 2, 4, and 10. Nonetheless, in BEP simulations, $\Delta U(\mathrm{TKE\text{-}ACM2} - \mathrm{Boulac})$ was a maximum over urban grids at approximately 2 to 4 times H_{max}, compared with approximately about 5 times H_{max} in Bulk simulations.

~~The trends of $\Delta U(\mathrm{BEP} - \mathrm{Bulk})$ are found similar in the two schemes. The height at which $\Delta U = 0$ is generally observed at $\sim 300\,\mathrm{m}$, corroborating what has been observed in Berlin, Munich, and Prague by Karlický et al. (2018). Below $z(\Delta U = 0)$, BEP consistently reduces U by $\sim 1 - 2\,\mathrm{m/s}$, and $\Delta U(z)$ generally exhibits a monotonically descending trend from the ground level. Nonetheless, TKE-ACM2+BEP shows slightly lower $z(\Delta U = 0)$. In addition, it shows a consistently greater reduction in ΔU at the height close to the ground than Boulac+BEP in all urban grids. Another distinction is that TKE-ACM2+BEP seems to accelerate U slightly more than Boulac+BEPfrom $z(\Delta U = 0)$ to approximately $800\,\mathrm{m}$. Both BEP simulations produce less profound differences in U over the water surfaces and the natural land cover than over urban grids.Fig. 8 displays the variation of $\Delta\theta(\mathrm{BEP} - \mathrm{Bulk})$, which is found to increase from negative values at the ground level to nearly zero beyond $z(\Delta\theta(\mathrm{BEP} - \mathrm{Bulk})$ in TKE-ACM2+BEP but shows a persistently negative value in Boulac+BEP. In the absence of anthropogenic heat modeled in BEP +BEM, the buildings behave as a sink of heat in the lower part of PBL by solely applying BEP.~~

4.2 Monthly mean diurnal profiles of U compared with high-resolution LiDAR measurements

~~Firstly, the~~ The monthly mean diurnal ~~variation of~~ variations of the heat flux, ~~Monin-Obkuhov~~ Monin-Obukhov length (L), and ~~the~~ stability parameter (h/L) are ~~displayed~~ presented in Fig.9. ~~The~~ At the HT_rural LiDAR station, the heat flux pattern ~~does~~ did not exhibit a ~~visible differenceat the rural LiDAR station HT. At the LCZ 5 USTSS~~notable difference. However, the USTSS_LCZ5 LiDAR location, introducing BEP consistently ~~exerts~~ resulted in a greater surface heat flux ~~than~~ compared with the Bulk methods. In contrast, ~~the magnitude of surface heat flux at the LCZ 1 KPLiDAR location has been reduced in the~~

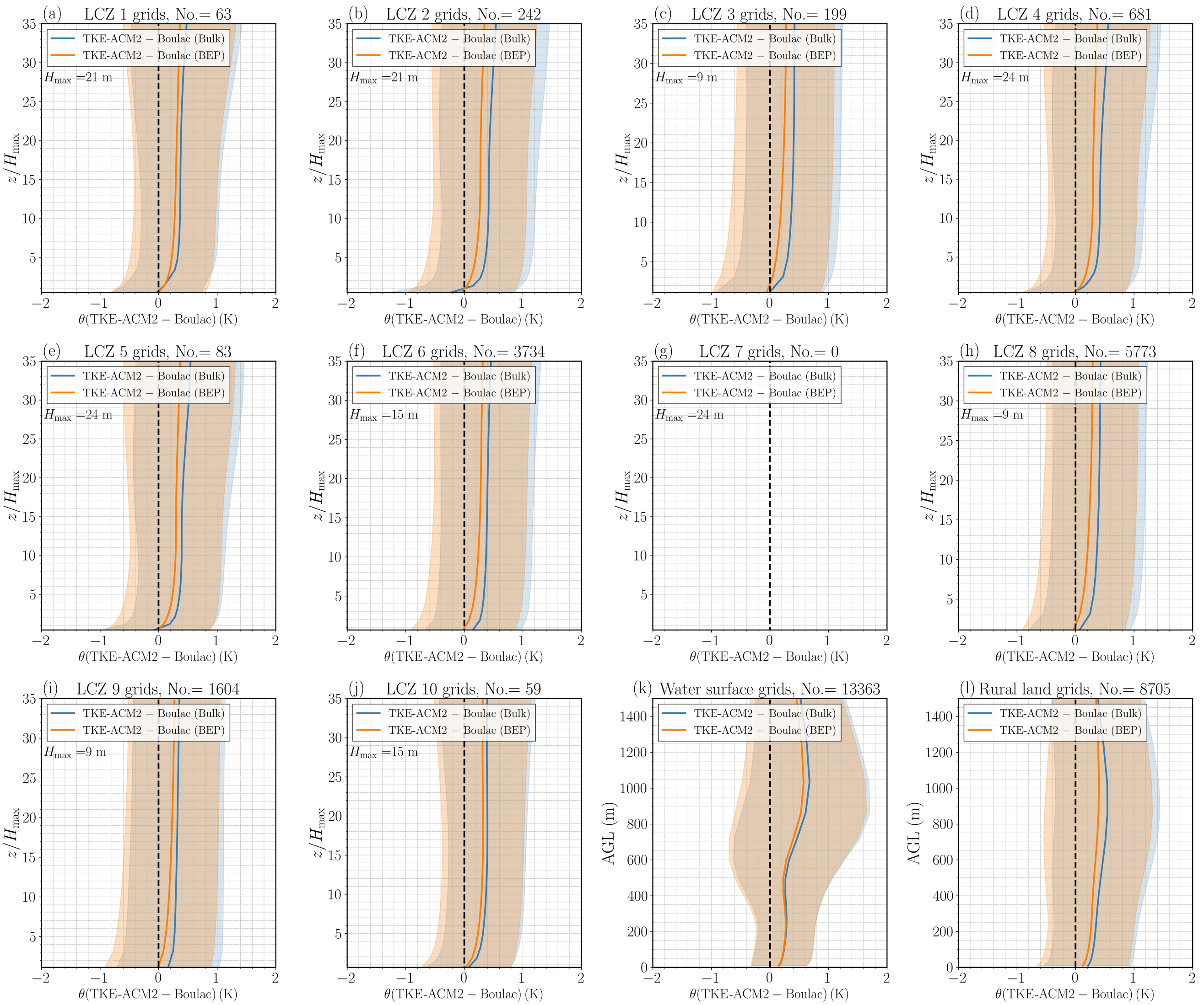

~~a-j): Monthly mean vertical profiles of ΔU over LCZ 1-10; k): over water surfaces; l): over other natural landuse. The shadowed area denotes $\pm 1\sigma$ variability.~~

Figure 7. a-j): Monthly mean vertical profiles of $\Delta\theta$(TKE-ACM2 – Boulac) with/without BEP over LCZ 1-10 (urban) grids; k): over water surface girds; l): over rural land cover grids. The blue and orange lines represent BEP and Bulk simulations, respectively. The shadowed area denotes $\pm 1\sigma$ variability. The height is normalized relative to the maximum building height ($H_{\max}$) for a specific urban LCZ type.

~~entire diurnal cycle. The surface station located in the proximity of the KP LiDAR site suggests that the observed T_2 (shown in Fig.A51) is constantly higher than the prescribed building and street temperature, which can justify that the reduction of~~

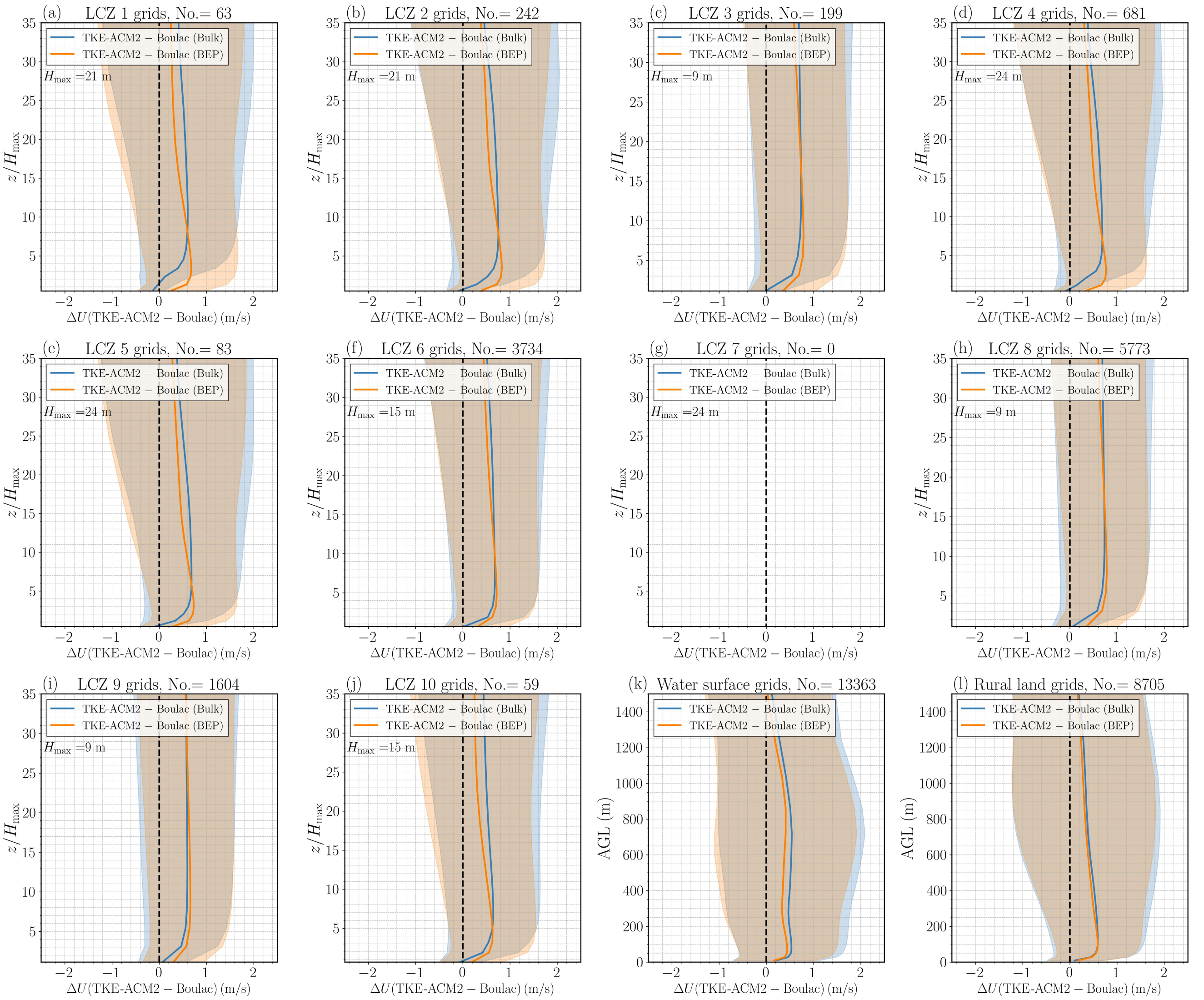

Figure 8. a-j): Monthly mean vertical profiles of ~~$\Delta\theta$~~ ΔU(TKE-ACM2 – Boulac) with/without BEP over LCZ 1-10 (urban) grids; k): over water ~~surfaces~~surface girds; l): over ~~other natural landuse~~rural land cover grids. The blue and orange lines represent BEP and Bulk simulations, respectively. The shadowed area denotes $\pm 1\sigma$ variability. The height is normalized relative to the maximum building height ($H_{\max}$) for a specific urban LCZ type.

~~modeled~~ at KP_LCZ1, BEP simulations produced a lower surface heat flux ~~is caused by the sink of buildings when BEP is activated~~throughout the diurnal cycle.

The wind speed LiDAR offers hourly measurements of wind speed at an altitude of 50 m ~~above ground level (AGL)~~AGL, with vertical increments of 25 m. The measured and simulated wind speed profiles ~~are averaged during~~ averaged across

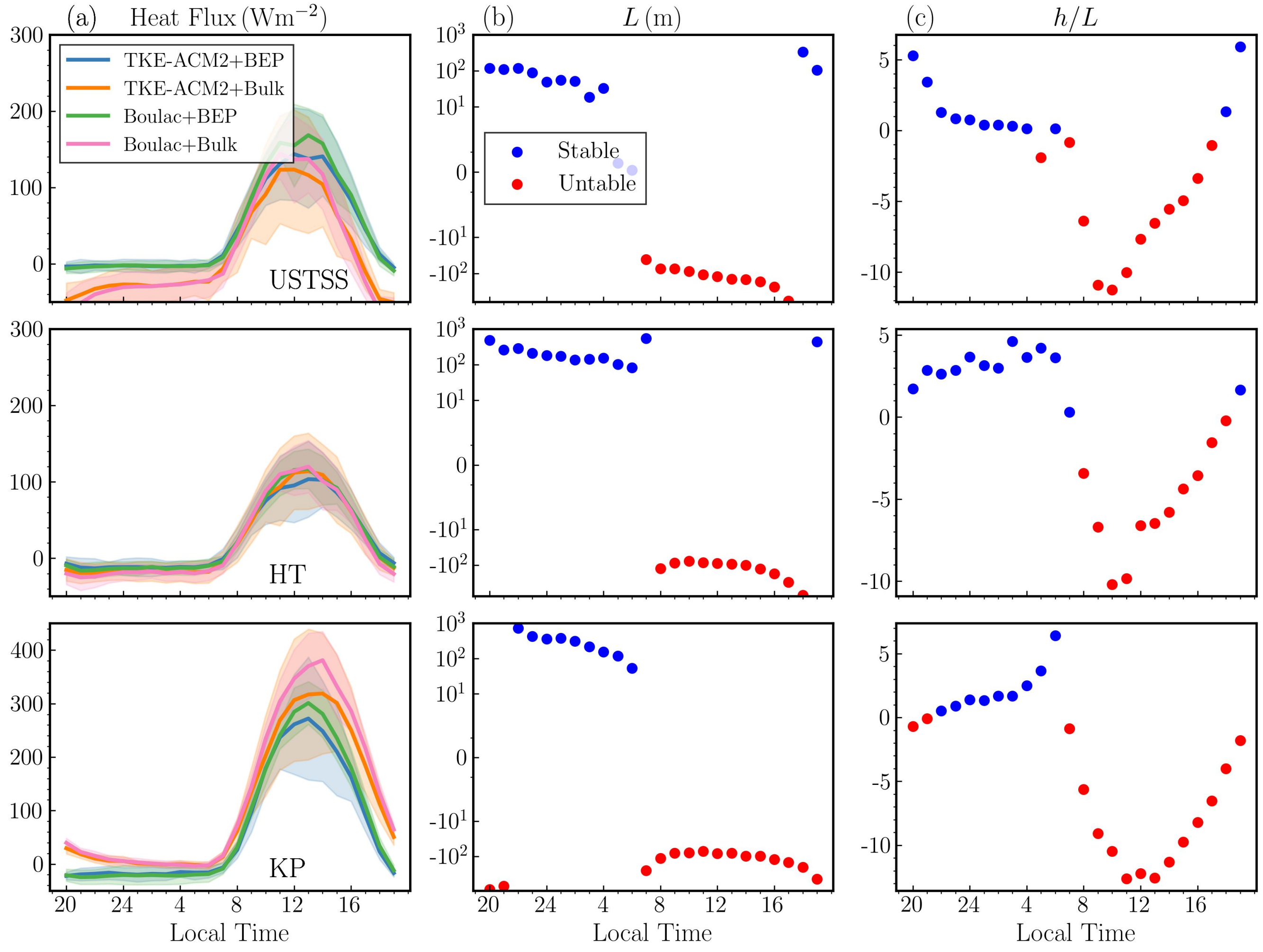

Figure 9. Column a) ~~plots the~~ monthly mean diurnal ~~pattern~~ patterns of the surface heat flux ~~at~~ for USTSS_LCZ5, HT_rural, and KP~~in the first, second, and third row, respectively~~_LCZ1 from top to bottom; Column b) ~~the Monin-Obkuhov~~ Monin-Obukhov length (L) ~~in~~ with a semi-log $y-$axis; Column c) ~~the~~ stability parameter (h/L). The integration is from 2000 UTC+8 on 18th July in 2022 to 2000 UTC+8 on 18th August in 2022.

the whole month are presented for each hour ~~and are displayed~~ in Fig.10 (USTSS_LCZ5), Fig.11 (HT_rural), and Fig.12 (KP_LCZ1). To quantify the performance of each simulation, the RMSE and mean bias (MB) ~~are demonstrated~~ between the simulated profiles and LiDAR measurements are presented in Fig.13.

~~Despite the fact that USTSSis~~ Although USTSS_LCZ5 was located in a model grid ~~identified as LCZ 5 (open midrise)~~classified as open mid-rise, applying BEP ~~does not imply a consistent and noticeable reduction in the wind speed, which is inconsistent with an average reduction~~ did not consistently result in a notable reduction in wind speed. This contrasts with the average

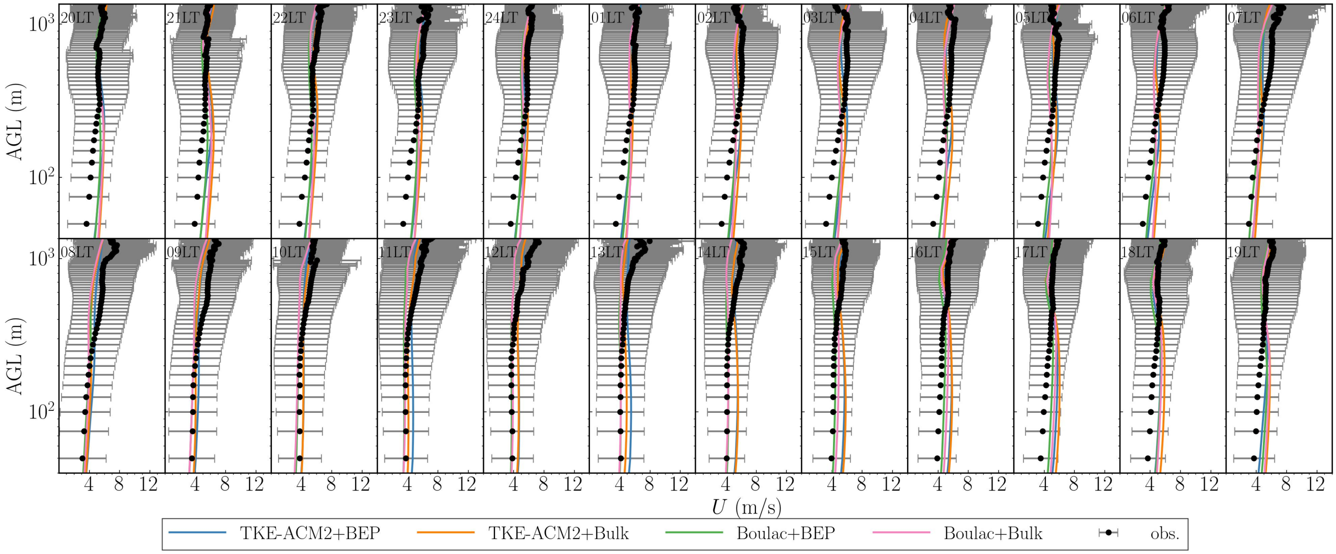

Figure 10. Monthly mean vertical profiles of wind speeds at the USTSS_LCZ5 LiDAR station. The blue, orange, green, and pink lines denote the results of TKE-ACM2+BEP, TKE-ACM2+Bulk, Boulac+BEP, and Boulac+Bulk, respectively. The black dots represent the ~~measurements from~~ LiDAR measurements, with the error bar ~~denoting~~ indicating the ±1 standard deviation. The integration is from 2000 UTC+8 on 18$^{\mathrm{th}}$ July in 2022 to 2000 UTC+8 on 18$^{\mathrm{th}}$ August in 2022.

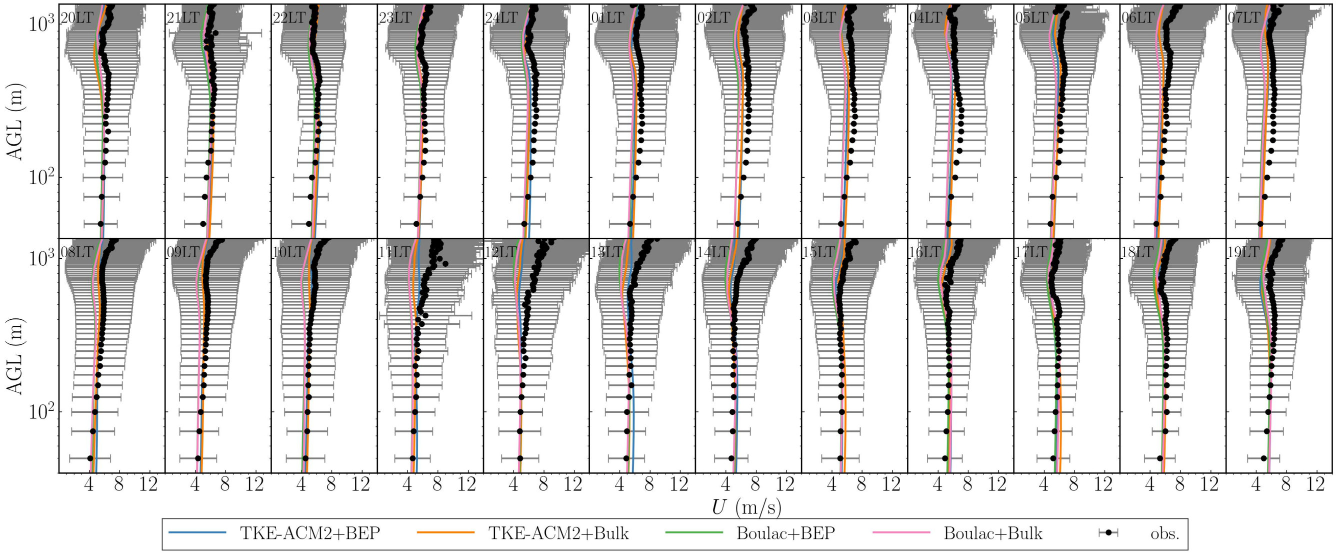

Figure 11. Same as Fig.10 but ~~at~~ for the HT_rural LiDAR station.

decrease of $\sim 1-2\,\mathrm{m/s}$ ~~found in~~ observed across all LCZ 5 grids, as shown in Fig.~~7~~C2e. A ~~closer inspection reveals that~~

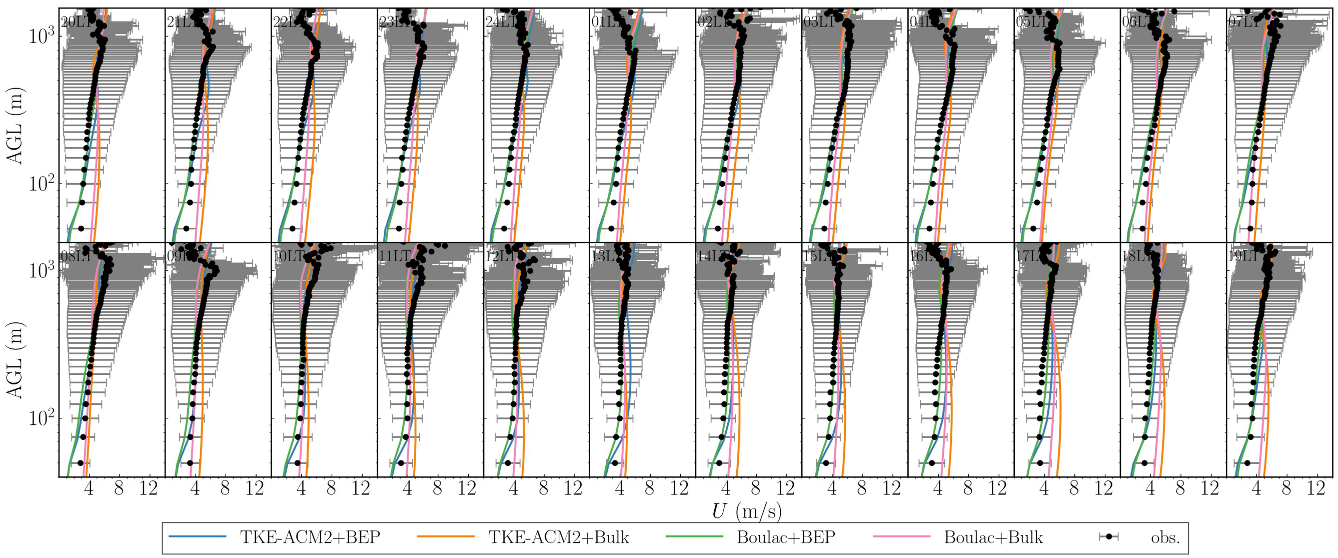

Figure 12. Same as Fig.10 but ~~at~~ for the KP_LCZ1 LiDAR station.

~~ΔU(BEP − Bulk) is found to be less visible in both PBL schemes compared to that observed at another urban LiDAR station KP (LCZ 1). A~~ possible explanation is that the LCZ map in Fig.2b indicates that the model grid containing USTSS~~is~~ _LCZ5 was bordered by either ~~natural~~ rural land or water grids, effectively isolating it from other urban grids. Consequently, the wind approaching this grid ~~experiences~~ experienced a less rough fetch, leading to a reduced drag exerted on this model grid. ~~It is found that the overprediction occurs~~ The overprediction occurred primarily below ∼300 m during the ~~nighttime~~ night for all schemes, with BEP simulations producing a slightly smaller positive bias. The overestimation below ∼300 m ~~persists~~ persisted in TKE-ACM2+BEP ~~during 11LT-17LT~~from 11 local time (LT) to 17LT, whereas Boulac+BEP ~~aligns better~~ aligned better with observations. Furthermore, all schemes ~~exhibit~~ exhibited underestimation above ∼300m. ~~Corroborating the accelerated ΔU above $z(\Delta U = 0)$ as~~ Consistent with the accelerated wind speed shown in Fig.~~7~~C2, TKE-ACM2+BEP ~~produces gently~~ produced slightly larger U beyond ∼300m, ~~which leads to the least positive bias compared to~~ leading to the smallest positive bias relative to the LiDAR observations. ~~It also should be highlighted that the~~ The accelerated U observed in the upper PBL ~~is also manifested~~ was also evident in the 10WC and 24SC idealized cases (Fig.4b & ~~d). Lastly, a detailed investigation~~ 4bd). Finally, detailed analysis reveals that the wind speed profiles during the ~~nighttime show~~ night showed less difference between ~~each scheme compared to~~ schemes compared with U simulated during the ~~daytime~~day. This is ~~likely due to~~ probably because TKE-ACM2 and Boulac ~~adopting a~~ adopt similar turbulence closure ~~model, and~~ models; their performance may differ less when there is an absence of convective ~~thermal~~thermals. In summary, the ~~RMSE~~ histograms in Fig.13 show that TKE-ACM2+BEP ~~produces the least~~ yielded the smallest RMSE and the ~~least~~ smallest negative MB, ~~in contrast to~~ whereas Boulac+BEP ~~further worsened the negative MB compared to~~ led to greater deviations compared with Boulac+Bulk.

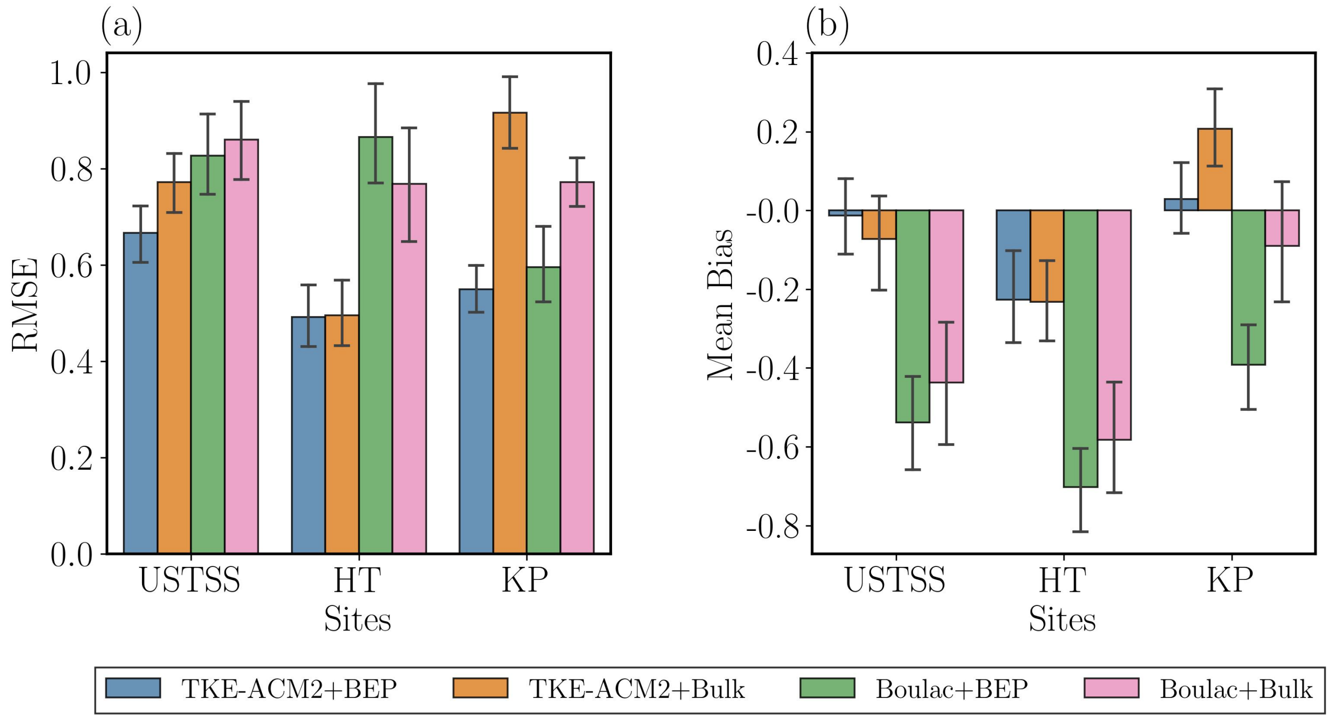

Figure 13. RMSE (a) and MB (b) of the monthly averaged diurnal variation of vertical profiles of wind speeds calculated at the three LiDAR stations for four simulations obtained by taking LiDAR measurements as the ground truth. The error bars represent the ±1σ variability of the RMSE/Mean bias of a diurnal cycle.

At the rural LiDAR station HT_rural, the application of BEP ~~has~~ had a limited impact on the PBL performance over non-urban model grids, ~~aligning with~~ supporting the conclusion drawn in Section ~~4??~~4.1. The differences between BEP and Bulk ~~are~~ were indistinguishable below $\sim 400\,\mathrm{m}$. However, TKE-ACM2+BEP occasionally ~~accelerates~~ accelerated U ~~notably~~ beyond $\sim 600\,\mathrm{m}$, ~~for instance,~~ such as from 10LT to 13LT, ~~matching closer to~~ aligning more closely with LiDAR observations. ~~Conclusively, BEP causes minor differences~~ Overall, BEP introduced only minor variations in U profiles ~~at~~ within non-urban model grids, particularly in the lower PBL. Therefore, the differences in the ~~predictability~~ accuracy of U within this height range over non-urban grids ~~are~~ were largely caused by the PBL schemes rather than the UCMs. Nonetheless, ~~the influence of BEP could be slightly more profound~~ BEP had a slightly more pronounced effect in TKE-ACM2+BEP by accelerating U in the upper PBL~~in TKE-ACM2+BEP, which leads to an~~ , leading to the improved reproduction of U profiles at HT_rural LiDAR station. ~~Unlike the USTSSstation~~ In contrast with the USTSS_LCZ5 station, which was located in an isolated LCZ 5 grid, ~~KP is deployed in the well-developed~~ the KP_LCZ1 station was situated in the densely developed downtown area of Hong Kong~~. The two~~ , surrounded by an extensively built-up environment. Both schemes coupled with BEP ~~exhibit~~ exhibited considerably decelerated wind speeds below $\sim 400\,\mathrm{m}$, ~~collaborating Fig.7a. It should be highlighted that discrepancies are diminished mainly from~~ corroborating the trend observed for all LCZ 1 girds shown in Fig.C2a. Notably, discrepancies were reduced within $100-400\,\mathrm{m}$ ~~where Bulk methods predict visibly overestimated wind speeds~~ range, where wind speeds tended to be overestimated. However, BEP ~~tends to over-reduce the~~ tended to excessively reduce wind speeds in both schemes from 50 to $100\,\mathrm{m}$~~which corresponds to approximately $2.5-5H$~~, approximately 2.5 to 5 times $H_{\max}$ for this LCZ type, particularly ~~at heights closer to the~~ closer to ground level. In contrast, ~~Bulk methods produce~~ the Bulk methods produced bias of similar magnitudes but with a reverse sign below $100\,\mathrm{m}$. ~~From~~ In the $600-1000\,\mathrm{m}$ range, Boulac+BEP ~~exhibits~~ gave the lowest wind speeds during the ~~daytime and is comparable with~~ day and yielded wind speeds comparable to those of TKE-ACM2+BEP ~~during the nighttime~~at night. Moreover, the performance of TKE-ACM2+BEP ~~differs~~ differed from that of Boulac+BEP ~~between~~ in the $600-1000\,\mathrm{m}$ ~~by generating~~ range in that it generated a less negatively biased wind speed at particular hours, ~~e.g.,~~ such as from 08LT to 12LT. ~~Holistically~~Overall, the two PBL schemes coupled with BEP ~~lead to considerably improved RMSE compared to~~ had a considerably better RMSE than the Bulk methods at this particular compact high-rise grid. More specifically, TKE-ACM2+BEP ~~significantly outperforms~~ outperformed TKE-ACM2+Bulk, reducing the RMSE from $0.92\,\mathrm{m/s}$ to $0.55\,\mathrm{m/s}$ and reducing the MB from $0.21\,\mathrm{m/s}$ to $0.03\,\mathrm{m/s}$. ~~Additionally~~In addition, TKE-ACM2+BEP ~~demonstrates slightly better performance~~ performed slightly better than Boulac+BEP~~of which RMSE is~~, which had an RMSE of $0.60\,\mathrm{m/s}$.

4.3 ~~Effects~~ Impact of ~~BEP~~ TKE-ACM2 on U_{10}, T_2, and RH$_2$~~over different LCZ types~~

~~The~~ Figures C3, C4, and C5 present the diurnal patterns of U_{10}, T_2, and ~~2 m~~ 2-m relative humidity (~~RH$_2$) simulated by the four schemes are demonstrated in Fig. A3, Fig.A4, and Fig.A5, respectively. Fig.14 , Fig.15 , and Fig.16 display the differences between BEP and Bulk simulations in monthly averaged~~ RH2) simulated using the four configurations. The impact of TKE-ACM2 on these surface meteorological variables, relative to Boulac, was examined in simulations with and without BEP, as shown in Figs.14 (U_{10}~~,~~), 15 (T_2~~, and~~), and 16 (RH$_2$~~by grouping into different LCZ types. It is found that BEP generally reduces~~).

Notably, the difference in U_{10} ~~in urban grids. Boulac suggests ΔU_{10} follows an evident diurnal pattern while TKE-ACM2 shows a less profound one with a different phase. In general, ΔU_{10} simulated by Boulac reaches the minimum absolute value at approximately 10LT. In this case, $|\Delta U_{10}|_{\min}$ can be as low as zero.In contrast, $|\Delta U_{10}|_{\min}$ is more likely to be found at around 06LT in~~ between TKE-ACM2 and Boulac was greatest at 12LT, aligning with the peak sensible heat flux (Fig.9a). This deviation arose because TKE-ACM2 ~~, where its magnitude is larger than Boulac. The diurnal pattern simulated by Boulac persists in the natural grids, and accelerated~~ incorporated non-local momentum transport that scaled with atmospheric instability, whereas Boulac adopted fully local momentum transport. However, incorporating BEP reduced this difference in urban grids, as BEP effectively lowered U_{10} ~~are observed during the daytime. ΔT_2 and $\Delta \mathrm{RH}_2$ exhibit evident diurnal variation which are negatively correlated due to the inverse proportionality. Unlike the ΔU_{10}~~ (Fig.C3). Specifically, TKE-ACM2+Bulk produced higher wind speeds than Boulac+Bulk during the day by up to $1\,\mathrm{m/s}$, a difference that diminished to less than $0.4\,\mathrm{m/s}$ with BEP integration.

Figure 15 shows that the temperature difference ΔT_2(TKE-ACM2 − Boulac) followed a diurnal pattern, ~~similar phases in ΔT_2 and $\Delta \mathrm{RH}_2$ are found between the two schemes. It is noticeable that Boulac+BEP may occasionally generate a warmer~~ with TKE-ACM2 consistently simulating lower T_2 ~~than Boulac +Bulk, e.g. ,~~ at ~~∼11 LT to~~ 12LT ~~over LCZ 2, 4,~~

~~and~~ relative to Boulac which aligns with the results of idealized simulations with a similar heat flux magnitude (Case 24SC depicted in Fig.4c). Importantly, with BEP, this temperature difference increased at noon, particularly across LCZ 1 to 5 grids~~,~~ ~~but TKE-ACM2+BEP consistently reduces T_2. Correspondingly, a drier atmosphere could be observed in Boulac+BEP than Boulac+Bulk, but RH_2 always increases in TKE-ACM2+BEP . Lastly, the three surface meteorological variables exhibit little sensitivity to surface layer fluxes parameterizations over water grids but can be gently altered at other natural grids~~. In contrast, $\Delta\mathrm{RH}_2$ remained positively skewed and further increased when BEP was applied.

4.4 Monthly mean diurnal patterns of U_{10}, T_2, and RH_2 compared with surface stations

~~The time series and metrics for each individual~~ Time series data for each station are provided in the supplementary material of Zhang (2024) for detailed visualization. The diurnal variations of U_{10}, T_2, and RH_2 for a total of 31 surface stations ~~are~~ were aggregated based on their LCZ classifications, ~~which are~~ as shown in Fig.17, Fig.18, and Fig.19, respectively. ~~The~~ RMSE histograms are ~~displayed~~ presented in Fig.20. ~~Applying BEP results in a significant reduction in~~ The adoption of BEP reduced U_{10}, which ~~is consistent~~ aligns with the trend observed in Fig.~~14~~ C3 for all LCZ urban grids. This reduction greatly ~~improves the predictions~~ improved the reproduction of U_{10} at LCZ 5, 6, and 8 stations, which ~~are landuse consisting of primarily~~ were primarily in areas with low- or mid-rise buildings at relatively low building density. ~~A closer inspection shows~~ Closer inspection reveals that the improvements ~~are more profound during the nighttime~~ were more profound at night over the aforementioned stations. Among these stations, TKE-ACM2+BEP ~~performs~~ performed the best or comparably to Boulac+BEP ~~by reaching~~ with an RMSE as ~~low~~ small as $1.0\,\mathrm{m/s}$. However, the ~~modeled wind speeds in BEP for~~ wind speeds simulated using BEP at LCZ 1~~(compact high-rise)~~, 2, 4~~(open high-rise)~~, and 10 ~~(heavy industry) stations are undesirably lower than the~~ stations were lower than observed values, particularly during the ~~daytime. The largely underestimated~~ day. The large underestimation of U_{10} at the LCZ 1 surface station ~~is consistent~~ aligns with the underestimation of U at ~~$25\,\mathrm{m}$ observed~~ $50\,\mathrm{m}$ at the KP_LCZ1 LiDAR station. ~~More specifically, the two BEP simulations produce~~ Specifically, both BEP simulations consistently produced $U_{10} \approx 1\,\mathrm{m/s}$ ~~constantly and exhibit~~ with an RMSE $1.7-2.4\,\mathrm{m/s}$, which ~~is consistently worse than that~~ was worse than the RMSE of Bulk methods (RMSE$\sim 1.5\,\mathrm{m/s}$). The excessive reduction in U_{10} is likely to be ~~caused by the mismatched local LCZ class~~ due to the mismatch between local LCZ classifcation ($100\,\mathrm{m}$ resolution) and re-gridded LCZ ~~class~~ classification ($1\,\mathrm{km}$ resolution) at LCZ 1, 4, and 10 stations, ~~which is also reported in (Ribeiro et al., 2021)~~reported by Ribeiro et al. (2021). For instance, the ~~KP surface station which is identified~~ surface station co-located with the KP_LCZ1 LiDAR, also classified as an LCZ 1 ~~class stationby WRF is deployed at the hill whose spatial scale is~~ station, was situated on a hill with a spatial scale of $50\,\mathrm{m}$. Therefore, the ~~exposure is~~ immediate surroundings of the KP surface station were relatively open and flat~~in the local vicinity of the KP surface station. As a consequence,~~ . Nonetheless, another source of discrepancy stemmed from the use of a look-up table to determine urban canopy parameters (UCPs). This approach overlooks the heterogeneity of UCPs within a given LCZ urban class, leading to results that are less accurate than those of a gridded UCP method (Sun et al., 2021). As highlighted by Shen et al. (2019), among the critical UCP factors, the urban fraction is important in simulating horizontal wind speeds. However, the current study did not account for the variability of the urban fraction or the distribution of building heights within specified LCZ urban classes. As a result, the ~~model simulated U_{10} is largely underpredicted and not representative enough~~

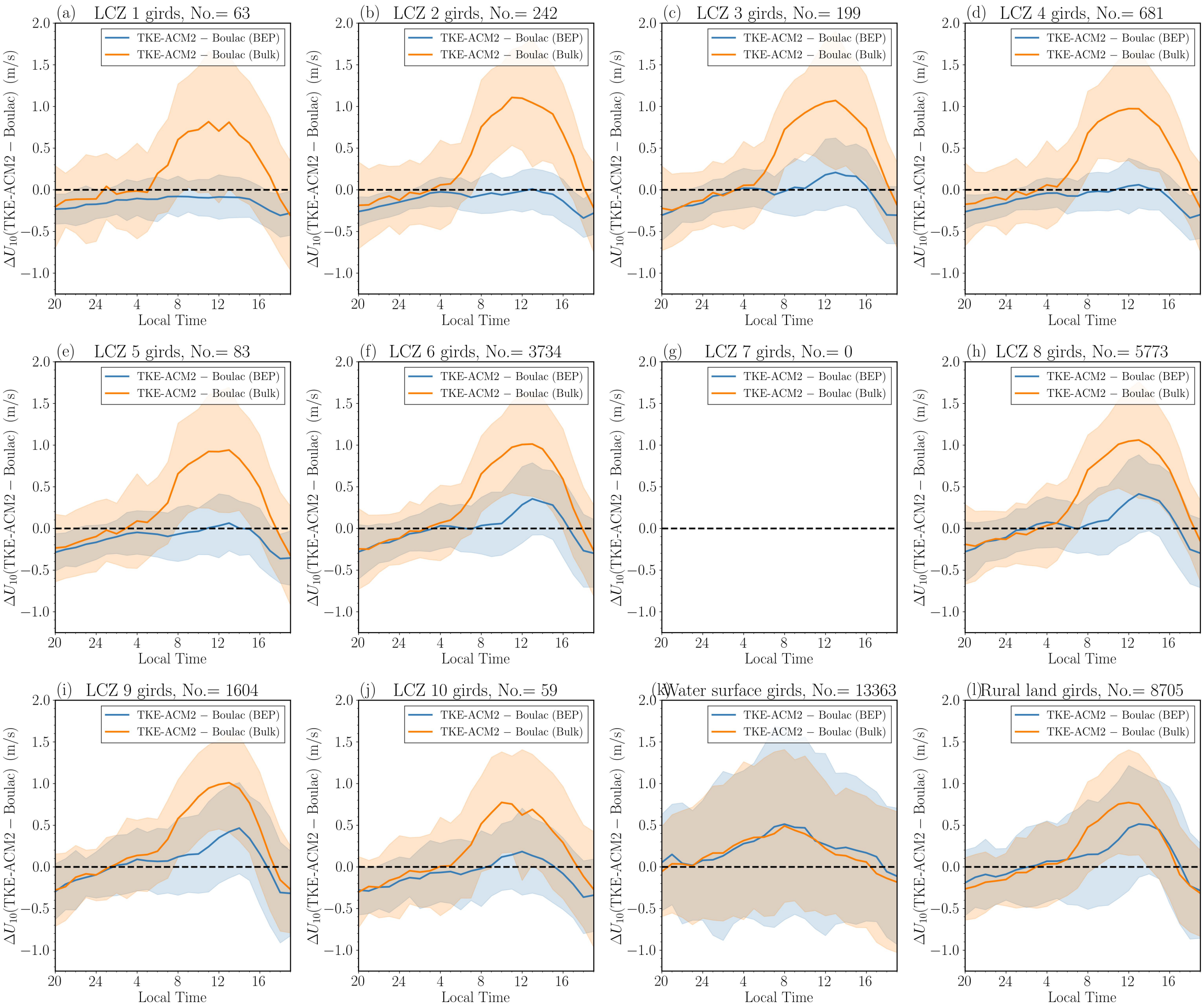

Figure 14. a-j): Monthly mean ~~ΔU_{10}~~ ΔU_{10}(TKE-ACM2 – Boulac) over LCZ 1-10 (urban) grids; k): over water ~~surfaces~~surface grids; l): over ~~other natural landuse~~rural land cover grids. The blue and orange lines represent the results of BEP and Bulk simulations, respectively. The shadowed area ~~denotes~~ indicates ±1σ variability.

~~at the exact location of the station. Lastly, it is observed that BEP coupled with the two schemes causes subtle differences to~~ model underestimated U_{10}~~at non-urban stations, but the slightly decreased wind speeds match better with observations at stations located on water surfaces by reducing RMSE by ∼0.2m/s~~, suggesting potentially poor representativeness at the station's exact location.

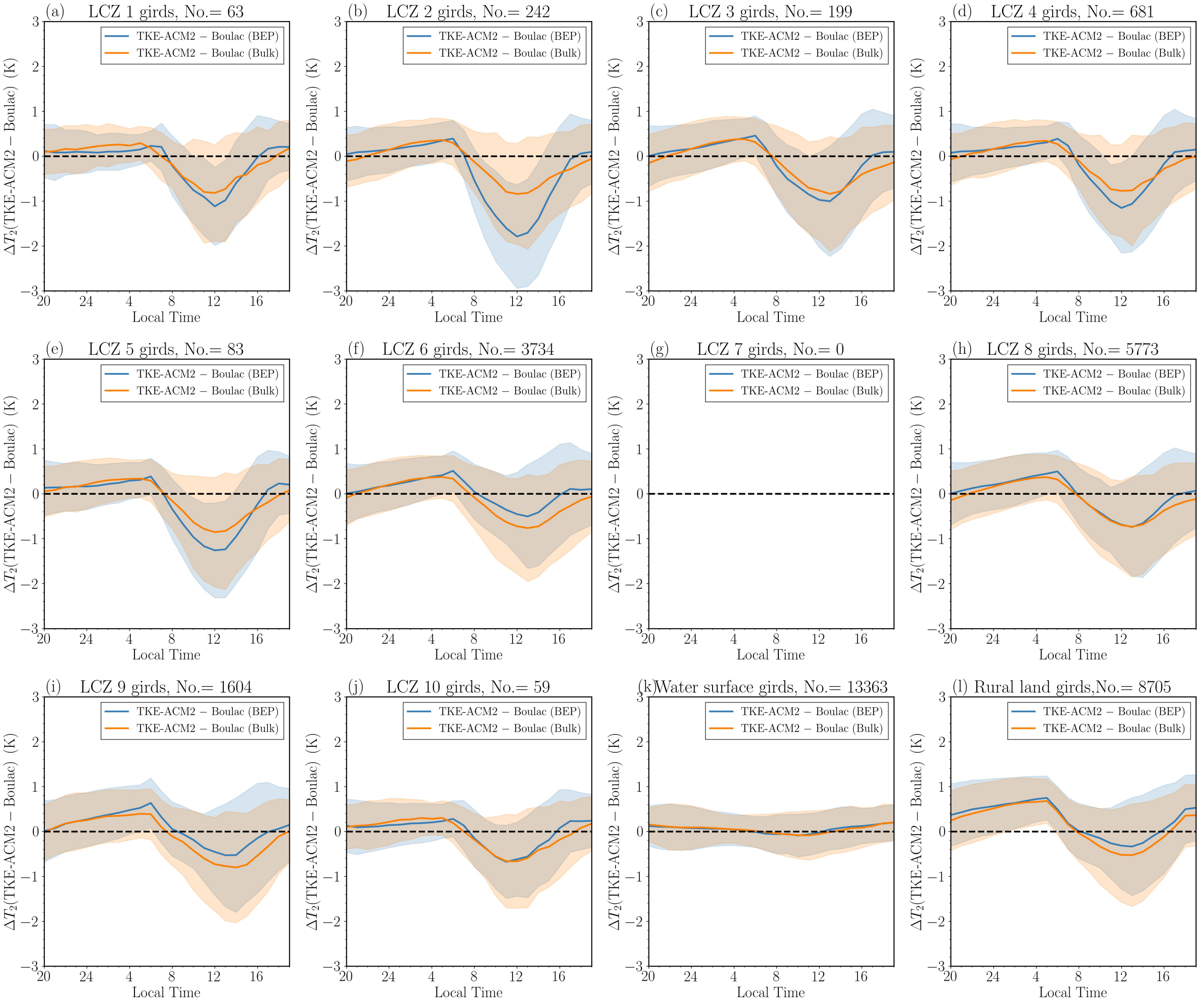

Figure 15. Same as Fig.14 but for T_2.

~~Coinciding with Fig.15,~~ Figure C4 shows that T_2 at ~~nighttime has been~~ night was reduced in BEP simulations over all LCZ urban stations. The change in T_2 ~~at daytime is less profound~~was smaller during the day, and Boulac+BEP ~~is~~ was likely to produce a warmer daytime T_2 ~~compared to~~ than TKE-ACM2+BEP. As a result, ~~both PBL schemes coupled~~ the coupling of either PBL scheme with BEP considerably ~~improve~~ improved the warm bias at ~~nighttime compared~~ night relative to Bulk methods, and their ~~predictability at daytime changes insignificantly~~accuracy during the day hardly changed. TKE-ACM2+BEP ~~behaves visibly better than~~ outperformed Boulac+BEP over LCZ 2, 5, 8, and 10 stations, ~~where~~ with the RMSE(T_2) ~~is~~ reduced by 0.51 K, 0.13 K, 0.27 K, and 0.11 K, respectively. ~~Otherwise, their performance over~~ The performance in the two simulations

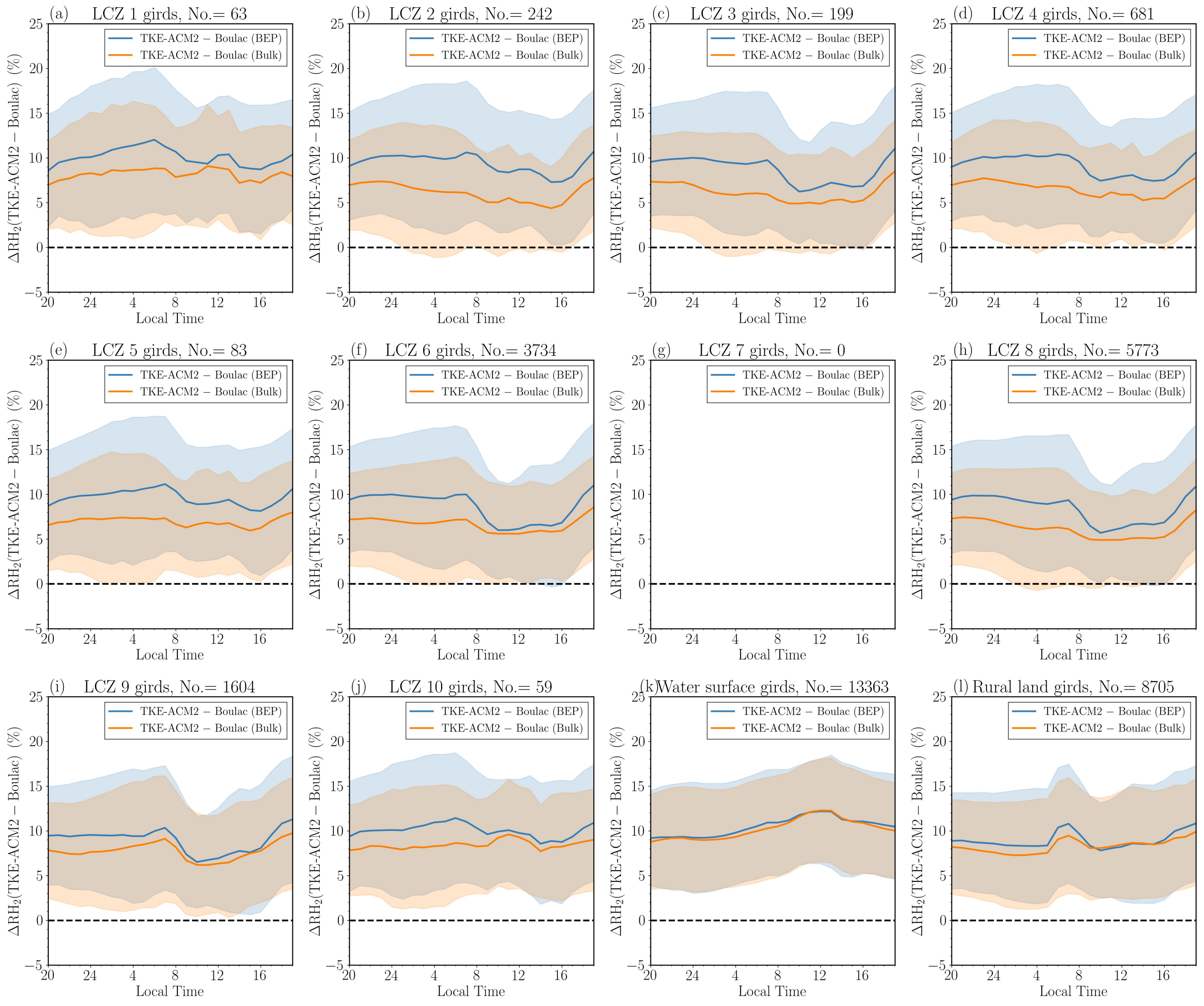

Figure 16. Same as Fig.14 but for RH_2.

was comparable for other LCZ urban stations~~is comparable~~. The four simulations ~~generate~~ generated T_2 diurnal cycles ~~of much less~~ with much lower amplitude than observations at water surfaces, where the inter-scheme difference ~~is~~ was marginal and each scheme ~~deviates by $\sim 2.0\,$K from observations . T_2 at rural stations is found to be constantly underestimated by all simulations, especially the reduction of nighttime~~ deviated from observations by $\sim 2\,$K. At rural land stations, T_2 ~~by BEP simulationstends to slightly worsen the underestimation.~~ was consistently underestimated across all simulations. This underestimation was slightly exacerbated at night in BEP simulations, probably due to the effects of adjacent urban grids.

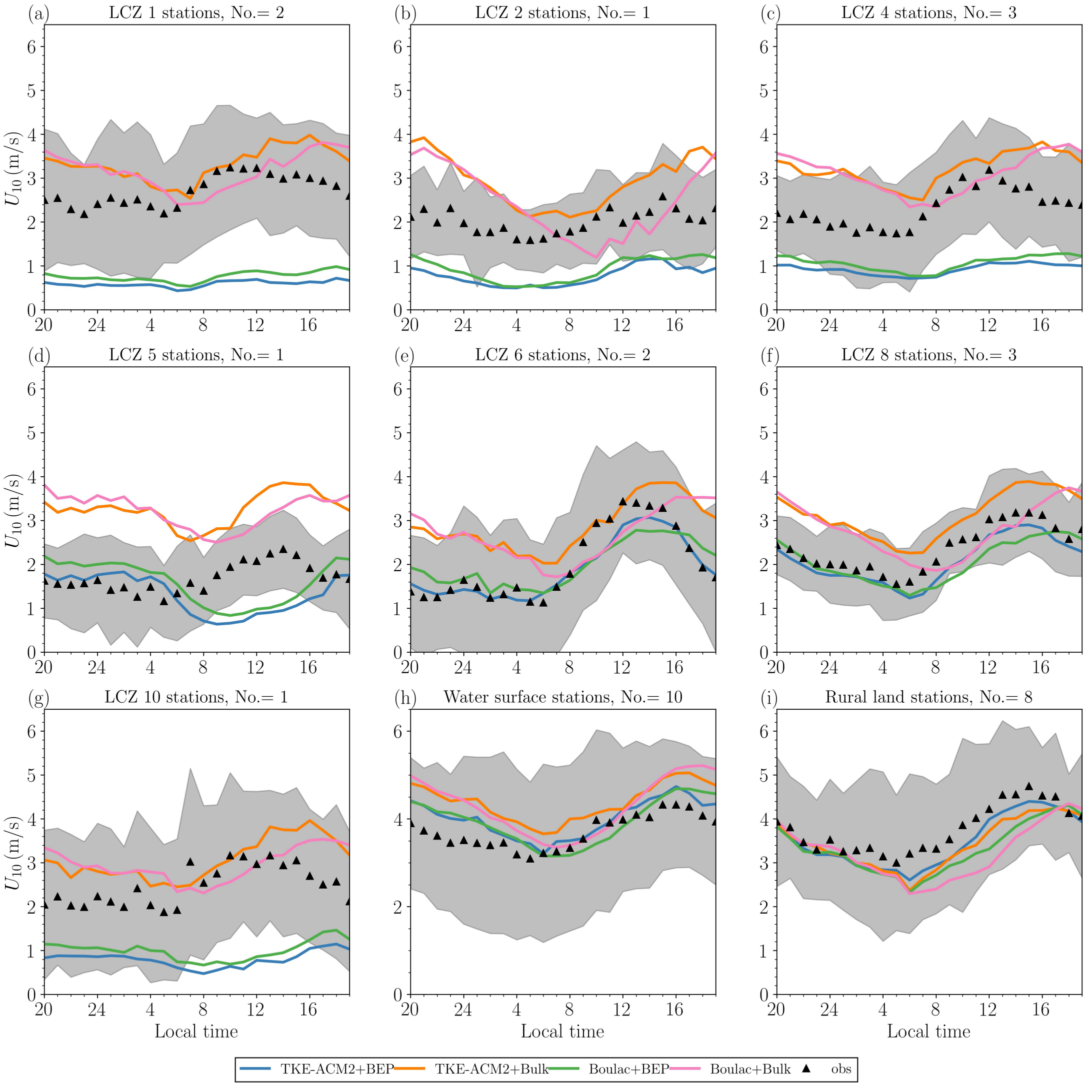

Figure 17. Comparison of monthly mean diurnal patterns of U_{10} with observations made at surface stations. The title of each panel describes the LCZ type and the ~~associated~~ number of associated surface stations. The blue, orange, green, and pink lines represent results of the TKE-ACM2+BEP, TKE-ACM+Bulk, Boulac+BEP, and Boulac+Bulk, respectively. The black ~~marker denotes~~ markers indicate the surface station observations. The gray shadowed area ~~displays~~ indicates the $\pm 1\sigma$ variability of observations.

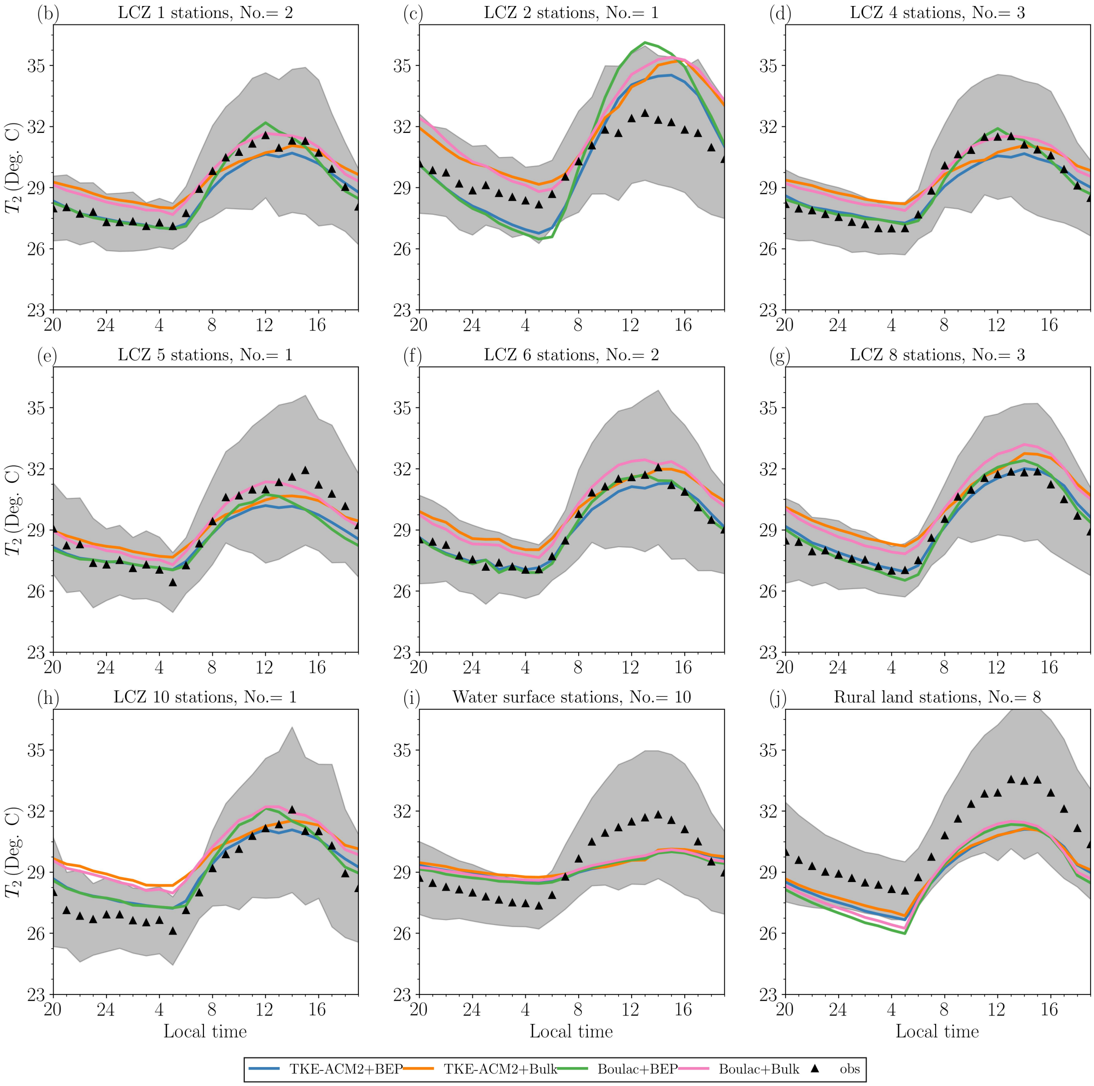

Figure 18. Same as Fig.17 but for T_2 comparison.

~~The trend of RH$_2$ is inversely proportional to that of T_2. It is found that Boulac always generates~~ Lastly, Boulac generated a much dryer boundary layer ~~at~~ than observations for all types of surface stations, regardless of the choice of surface layer flux parameterizations. ~~Likewise~~ Similar to Boulac+Bulk, TKE-ACM2-Bulk ~~produces~~ produced a dryer surface layer ~~though of~~ but with much less negative bias. The addition of BEP to the two PBL schemes ~~has~~ greatly improved the ~~predictability~~ accuracy

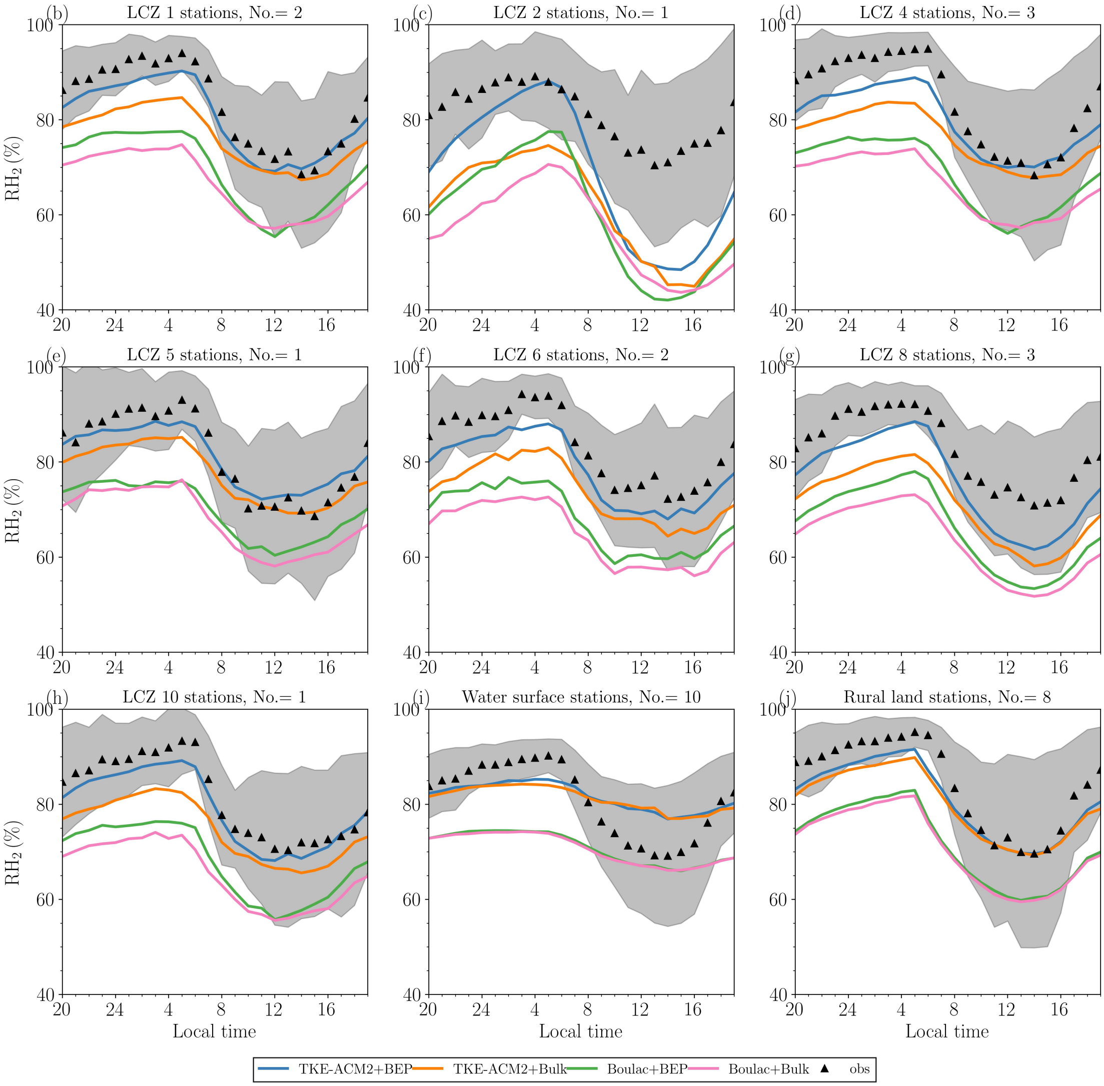

Figure 19. Same as Fig.17 but for RH$_2$ comparison.

of RH$_2$ at urban stations ~~, while the influence of BEP is relatively marginal on RH$_2$ at non-urban stations. Fig. 16 indicates that BEP implies a greater~~ by simulating moister air. Figure C5 shows that BEP produced an increasingly large RH$_2$ when coupled ~~to~~ with TKE-ACM2 ~~than to~~ rather than with Boulac, resulting in a more profound improvement in TKE-ACM2+BEP. In summary, BEP ~~does not only affect~~ affected not only the surface wind speed but ~~also has important implications on~~ the

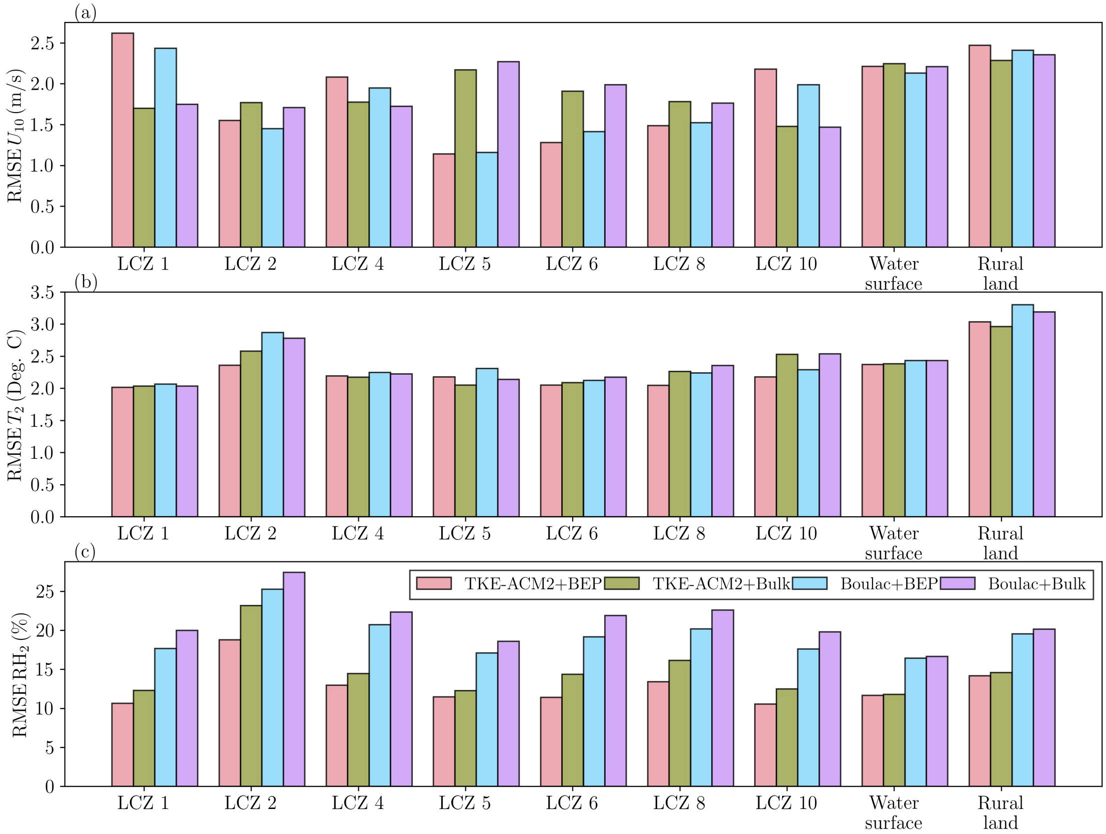

Figure 20. RMSE ~~at~~ for aggregated station types, with a), b), and c) ~~drawing for~~ representing U_{10}, T_2, and RH$_2$, respectively. The number of stations contributing to an LCZ type is given in the sub-titles in Fig.17, Fig.18, or Fig.19.

T_2 and RH$_2$ diurnal patterns. TKE-ACM2+BEP ~~has demonstrated superiority over~~ outperformed other schemes in ~~reducing the~~ terms of reducing warm bias at ~~nighttime~~ night and enhancing the ~~predictability of~~ accuracy in simulating RH$_2$ at urban stations.

580 5 Conclusions

In this study, we ~~have developed the numerical method to couple~~ developed a numerical method for coupling BEP with the TKE-ACM2 planetary boundary layer scheme detailed ~~in~~ by Zhang et al. (2024). We first evaluated the performance of TKE-ACM2+BEP under a series of idealized atmospheric conditions with a simplified urban morphology in ~~WRF. The~~ the

WRF model. We used a state-of-the-art large-eddy simulation tool, PALM, configured with three-dimensional equidistant resolution~~is utilized ,~~, to provide a reference result at the ~~building-resolved scale. It has been~~ building-resolving scale. We demonstrated that TKE-ACM2+BEP ~~significantly improves the reproduction of~~ outperformed TKE-ACM2 without an urban canopy model in reproducing the vertical profiles of θ and u in ~~the~~ two prescribed surface heat flux cases~~compared to~~. Moreover, TKE-ACM2~~without any urban canopy model, and it also shows superiority in the moderately convective case compared to another~~ +BEP outperformed the widely used Boulac+BEP scheme in the moderately convective case. In particular, TKE-ACM2+BEP ~~predicts~~ predicted θ with a reduced warm bias within the urban canopy layer. ~~Additionally~~In addition, Boulac+BEP ~~produces~~ produced a sharper $\partial\theta/\partial z$ at the roof level, leading to a ~~noticeable~~ notable cold bias in the mixed layer. ~~A closer inspection suggests~~ Closer inspection suggested that turbulent fluxes ~~are~~ were better reproduced by TKE-ACM2+BEP, which is attributable to ~~the~~ non-local fluxes. In contrast, Boulac+BEP ~~significantly underestimates~~ underestimated their magnitudes.

Real case simulations adopting different parameterization schemes for surface layer fluxes ~~parameterization schemes~~ were performed. ~~It is shown that~~ TKE-ACM2+BEP ~~exhibits similar behavior~~ behaved similarly to Boulac+BEP, ~~both of which reduce~~ with both reducing U below a certain height over the LCZ urban grids ~~. The heat flux computed from~~ relative to Bulk simulations. Likewise, the effects of BEP considering the radiative transfer and ~~conduction ultimately leads~~ sensible heat fluxes between solid surfaces and the atmosphere ultimately led to a lower ~~T_2 in this study~~θ over all urban grids. High-resolution wind speed LiDAR observations ~~are obtained and~~ were used to evaluate the performance of TKE-ACM2+BEP. ~~It is revealed that the reduction of~~ The reduction in U at USTSS~~(LCZ 5) is not constantly visible~~ _LCZ5 was not consistently observed across a diurnal cycle, which is ~~likely attributed~~ probably attributable to the fact that USTSS~~is~~ _LCZ5 was located in an isolated urban grid with a smoother fetch in all directions. BEP ~~has little impact on~~ hardly affected the wind speed profiles at the ~~rural LiDAR stationHT~~HT_rural station, where the four simulations ~~perform similarly. Lastly~~performed similarly. Finally, TKE-ACM2+BEP ~~demonstrates a considerably improved performance in predicting~~ outperformed TKE-ACM2+Bulk in reproducing vertical profiles of U at the LCZ 1 LiDAR station~~compared to TKE-ACM2+Bulk. The~~. In particular, the overestimation in the lower boundary layer ~~has been~~ was much improved. However, the wind speeds ~~are over-reduced~~ were overly reduced by BEP in Boulac and TKE-ACM2 below $\sim 100\,\mathrm{m}$. Overall, TKE-ACM2+BEP ~~outperforms others~~ outperformed other schemes in simulating the wind speed profile at this highly urbanized ~~grid. It should be pointed out that BEP does~~ LiDAR station.

BEP did not necessarily improve the prediction of U_{10} at all types of urban stations as it ~~can~~ could lead to largely underestimated U_{10} ~~compared~~ relative to the two schemes with Bulk methods~~, for~~. For instance, extremely low wind speeds ~~at~~ were observed at LCZ 1, 2, 4, and 10 stations, which were in areas that had mostly compact or high-rise buildings. The enhanced ~~predictability~~ accuracy of U_{10} simulated by TKE-ACM2+BEP ~~is noticeable~~ was notable at stations located in areas of relatively low building density, such as LCZ 5, 6, and 8 stations. The non-linear feedback to U_{10} at rural stations ~~can be~~ was slightly improved by TKE-ACM2+BEP, ~~where RMSE is reduced~~ with the RMSE reducing by $\sim 0.2\mathrm{m/s}$. ~~Therefore, it is~~ It is thus critical to select an appropriate configuration for simulating the wind speed ~~in the whole~~ throughout the boundary layer. Nonetheless, BEP ~~has~~ consistently improved the reproduction of T_2 for TKE-ACM2 over urban stations, particularly reducing ~~the~~ warm bias at ~~nighttime. The predicted~~ night. T_2 simulated by TKE-ACM2+BEP ~~is generally comparable with~~ was generally comparable to or slightly better than that simulated by Boulac+BEP at most urban stations. ~~On the other hand, RH_2 exhibits comparable sensitivity to PBL schemes and~~ Moreover, the sensitivity of RH_2 to PBL scheme was comparable to that to UCMs. BEP ~~leads to a more moist~~ led to moister PBL, and TKE-ACM2+BEP ~~exhibits~~ exhibited the least dry bias in reproducing RH_2 among all simulations. ~~This work does~~ The present work did not aim to demonstrate that the new TKE-ACM2+BEP performs definitively better ~~in simulating all aspects of the meteorological variables~~ than other combinations of PBL and UCM in simulating all aspects of meteorological variables; rather, it offers valuable insights for selecting appropriate model configurations to meet various objectives regarding different atmospheric processes.

Code and data availability. The PALM model is an open-source atmospheric LES model under the GNU General Public License (v3). (available at https://palm.muk.uni-hannover.de/trac, last access: November 2024). The WRF model encompassing the current version of TKE-ACM2 PBL scheme used to produce the results in this paper is archived on Zenodo (Zhang, 2024) under the Creative Commons Attribution 4.0 International license, as the data simulated by PALM and WRF for idealized and real simulations, LiDAR observations, and surface station observations (Zhang, 2024).

Appendix A: Numerical solutions to Eqn.3

Equation 3 can be solved by re-writing it as the linear system $\mathbf{A}\mathbf{x}=\mathbf{b}$, where the column vector $\mathbf{x}$ contains the unknown prognostic variable ζ_i^{n+1}, the square boarded band matrix $\mathbf{A}$ is the coefficient matrix, which comprises the first column entry ($\mathbf{E}$), diagonal ($\mathbf{D}$), upper diagonal ($\mathbf{U}$), and lower diagonal ($\mathbf{L}$) elements, and the column vector $\mathbf{b}$ comprises the explicit terms used in Eqn.3. To keep the same order of numerical accuracy as TKE-ACM2 (Zhang et al., 2024), the Crank-Nicolson scheme is retained. This splits ζ_i^{n+1} to $C\zeta_i^{n+1}+(1-C)\zeta_i^n$ with $C=0.5$ being the Crank-Nicolson factor. Subsequently, the element in the $i-$th row and $i-$th column of $\mathbf{D}$ is expressed as

$$\begin{aligned}\mathbf{D}_{i,i}&=1+Cf_{\text{conv}}\,\mathrm{Md}_i\Delta t\\&+C\left(1-f_{\text{conv}}\right)\frac{\Delta t}{\Delta z_i}\left(\frac{K_IS_I}{\Delta z_I}+\frac{K_{I-1}S_{I-1}}{\Delta z_{I-1}}\right)-CA_i\Delta t\end{aligned}\tag{A1}$$

The $i-$th row element of column vector $\mathbf{b}$ is expressed as:

$$\begin{aligned}\mathbf{b}_i&=\zeta_i^n+(1-C)f_{\text{conv}}\,\mathrm{Mu}\zeta_1^n\Delta t\\&-(1-C)f_{\text{conv}}\,\zeta_i^n\Delta t+(1-C)f_{\text{conv}}\,\mathrm{Md}_{i+1}\zeta_I^n\frac{\Delta z_{i+1}}{\Delta z_i}\Delta t\\&+\frac{1-C}{V_i\Delta z_i}f_{\text{conv}}\,(K_IS_I\frac{\zeta_{i+1}^n-\zeta_i^n}{\Delta z_I}\\&-K_{I-1}S_{I-1}\frac{\zeta_i^n-\zeta_{i-1}^n}{\Delta z_{I-1}})\Delta t+(1-C)A_i\zeta_i^n\Delta t+B_i\Delta t\end{aligned}\tag{A2}$$

The element in the $i-$th row and $j-$th column of $\mathbf{U}$, $\mathbf{L}$, and $\mathbf{E}$, are the same as those in Eqn.13, Eqn.14, and Eqn.15 in Zhang et al. (2024), respectively, except that an additional multiple of S_I/V_i applies to K_I.

Appendix B: LCZ classification and namelist configuration in WRF real case simulations

Table B1. ~~Configurations of WRF version 4.3.3 settings for simulations using Boulac and TKE-ACM2 PBL schemes and UCM schemes.~~Local Climate Zones (LCZ) classification scheme

LCZ code	Built type	Number of available surface stations	LCZ code	Land cover	Number of available surface stations
LCZ 1	Compact high-rise	2	LCZ A	Dense trees	4
LCZ 2	Compact mid-rise	1	LCZ B	Scattered trees	0
LCZ 3	Compact low-rise	0	LCZ C	Bush and scrub	3
LCZ 4	Open high-rise	3	LCZ D	Low plants	0
LCZ 5	Open mid-rise	1	LCZ E	Bare rock or paved	0
LCZ 6	Open low-rise	2	LCZ F	Bare soil or sand	1
LCZ 7	Lightweight low-rise	0	LCZ G	Water surface	10
LCZ 8	Large low-rise	3			
LCZ 9	Sparsely built	0			
LCZ 10	Heavy industry	1			
	Subtotal of urban stations	**13**		**Subtotal of non-urban stations**	**18**

Table B2. Configurations of WRF version 4.3.3 settings for simulations using Boulac and TKE-ACM2 PBL schemes and UCM schemes

WRF version 4.3.3 Options	Settings
Meteorological data for boundary and initial conditions	NCEP GFS 0.25° by 0.25° latitudinal and longitudinal resolution with 6-hour interval
Grid resolutions	27 km for D1 with 1:3 parent domain grid ratio for nested domains
Time steps	120 s for D1 with 1:3 parent time step ratio for nested domains
Number of grid points (East-West × North-South)	D1 283 × 184, D2 223 × 163, D3 172 × 130, and D4 214 × 163
Number of vertical eta levels	39
Pressure at top model level	50 hPa corresponding to approximately 20 km AGL
Number of vertical levels in WRF Preprocessing System (WPS) output	34
Number of soil levels in WPS output	4
Microphysics scheme	WSM 3-class simple ice scheme ~~Hong et al. (2004)~~ (Hong et al., 2004)
Longwave radiation scheme	RRTMG scheme ~~Iacono et al. (2008)~~ (Iacono et al., 2008)
Shortwave radiation scheme	RRTMG scheme ~~Iacono et al. (2008)~~ (Iacono et al., 2008)
Surface layer scheme	Revised MM5 Monin-Obukhov scheme ~~Jiménez et al. (2012)~~(Jiménez et al., 2012)
Land-surface scheme	Unified Noah land-surface model ~~Chen and Dudhia (2001)~~(Chen and Dudhia, 2001)
Cumulus scheme	Grell-Freitas ensemble scheme ~~Gall et al. (2013)~~(Gall et al., 2013)
Urban model (sf_urban_physics)	BEP (option 2) and Bulk (option 0)
Land-use data	LCZ (use_wudapt_lcz=1, num_land_cat=41)
Grid nudging	6-hour interval grid analysis nudging only for D1
Observational nudging	Off for all domains

Appendix C: θ and U profiles aggregated at different landuse

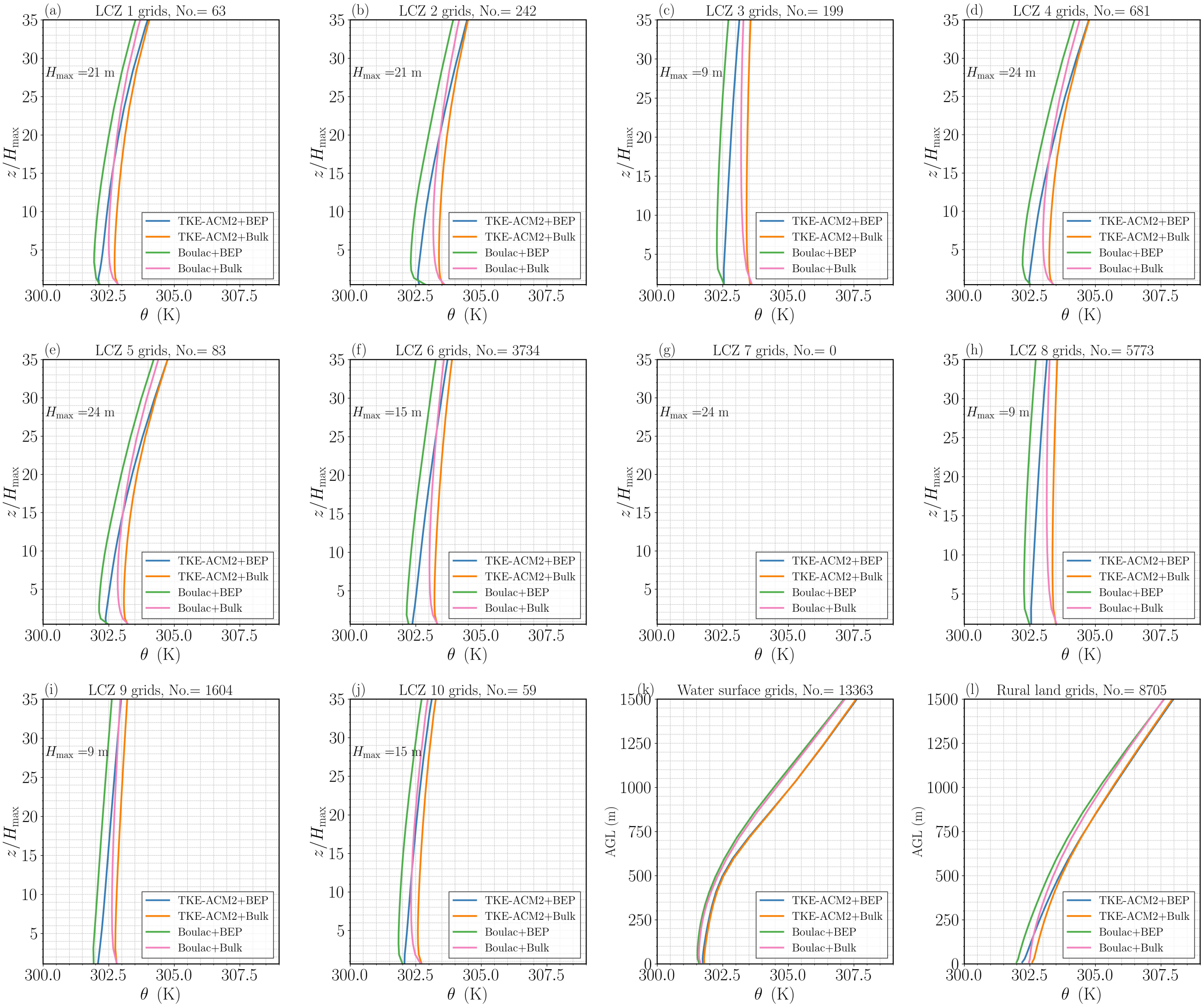

Figure C1. a-j): Monthly mean vertical profiles of θ over LCZ 1-10; k): over water surfaces; l): over ~~other natural landuse~~rural land cover.

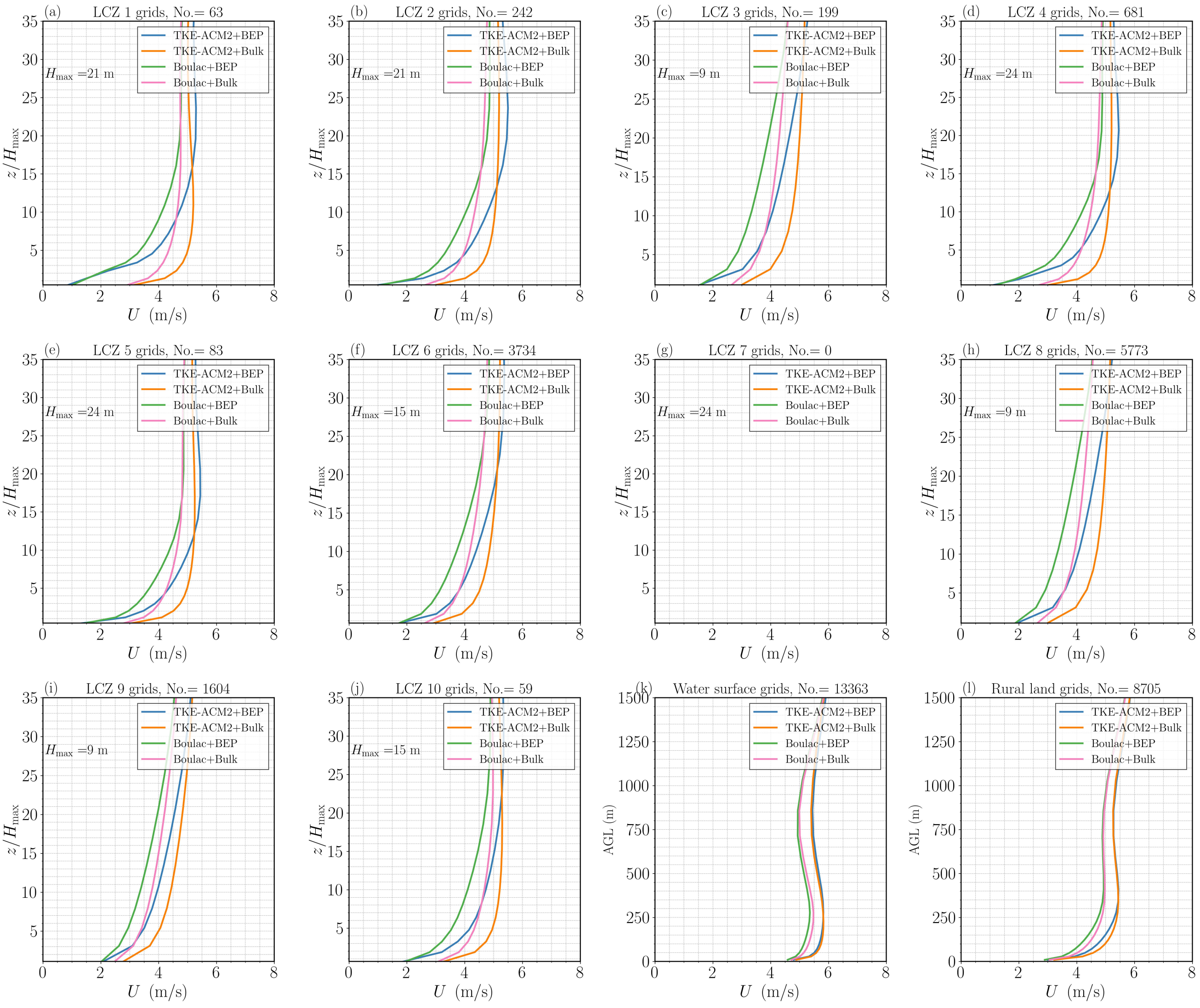

Figure C2. Same ~~to~~ as Fig.~~A1~~ C1 but for U.

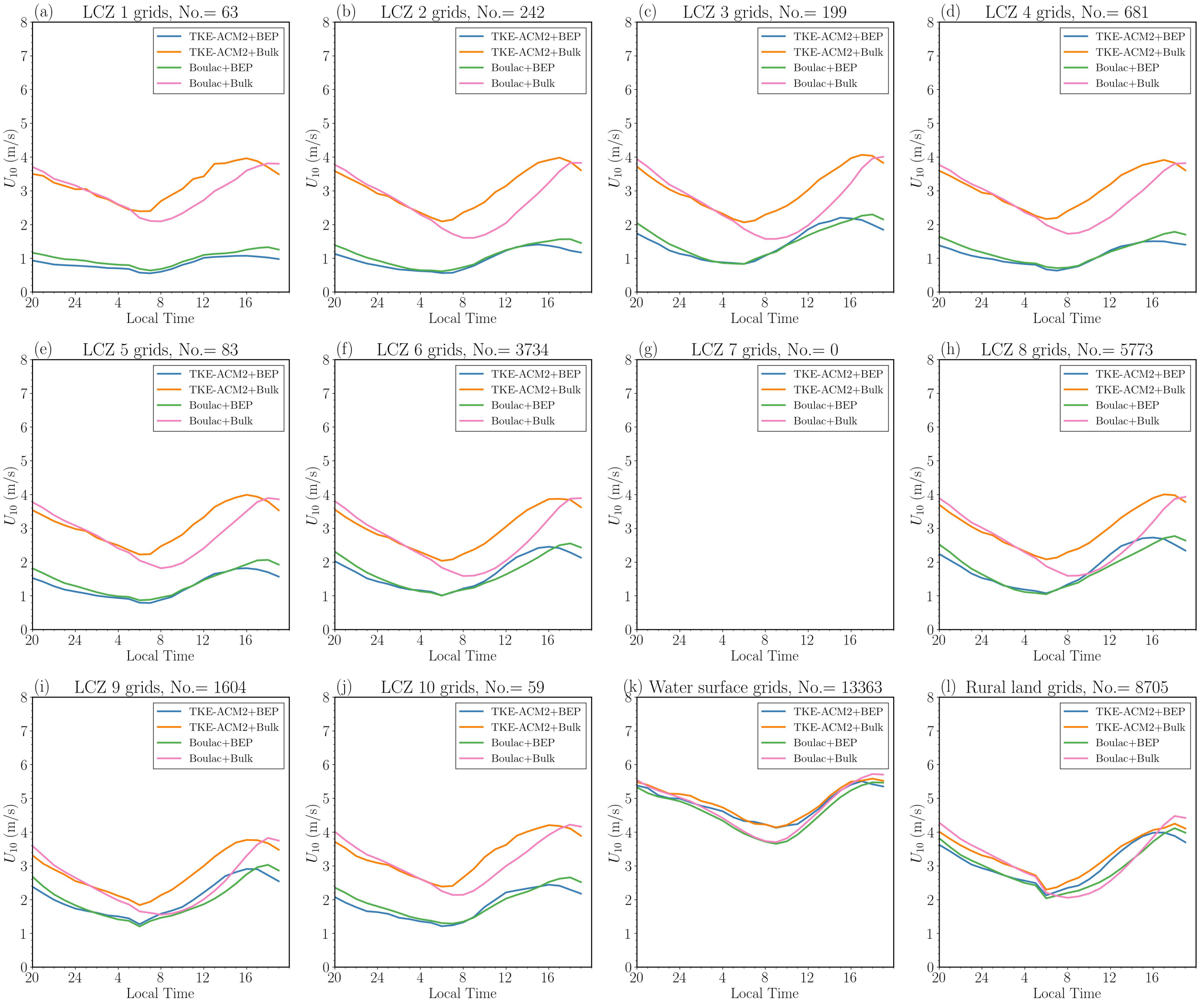

Figure C3. a-j): Monthly mean U_{10} over LCZ 1-10; k): over water surfaces; l): over ~~other natural landuse~~rural land cover.

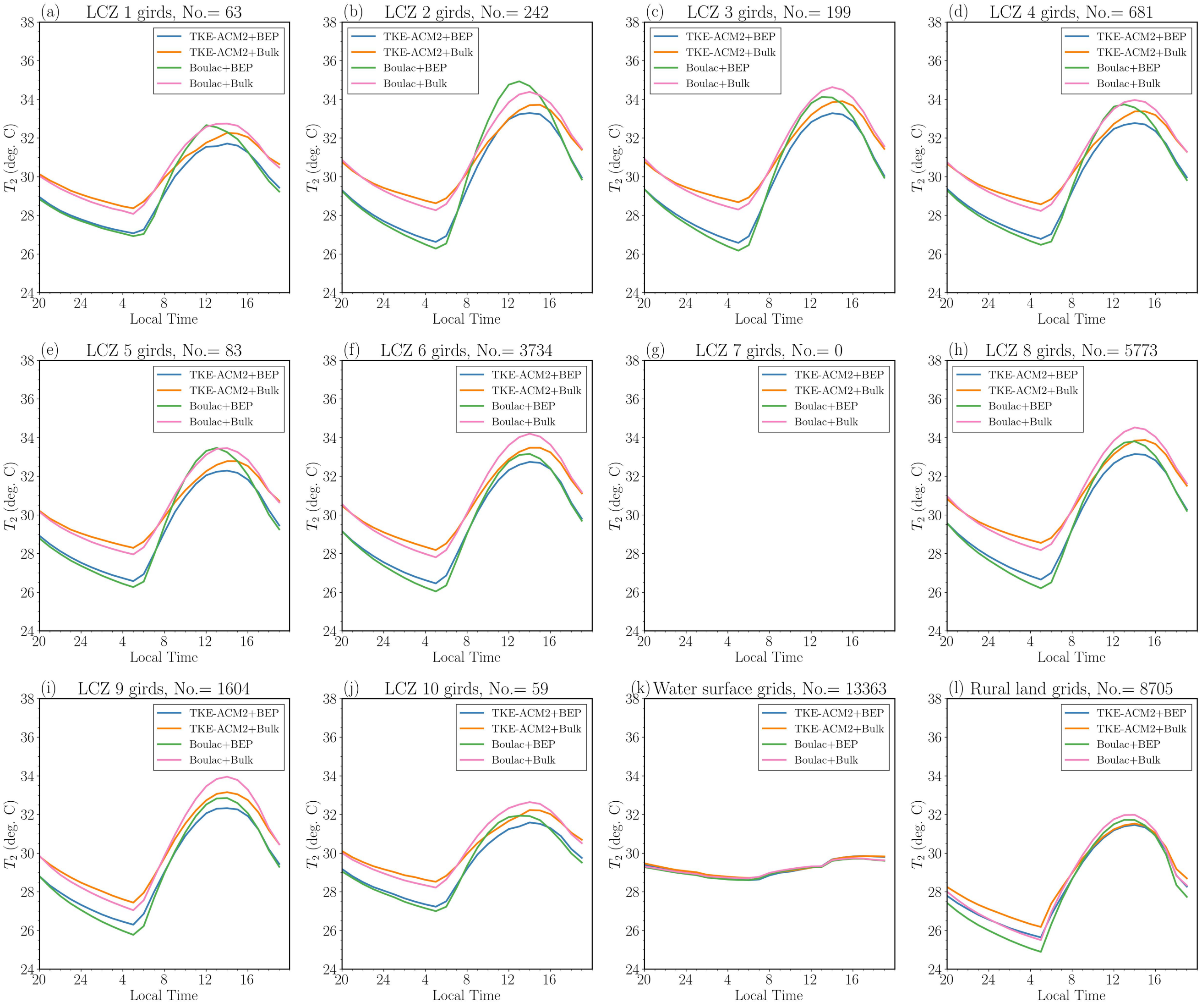

Figure C4. Same ~~to~~ as Fig.~~A3~~ C3 but for T_2.

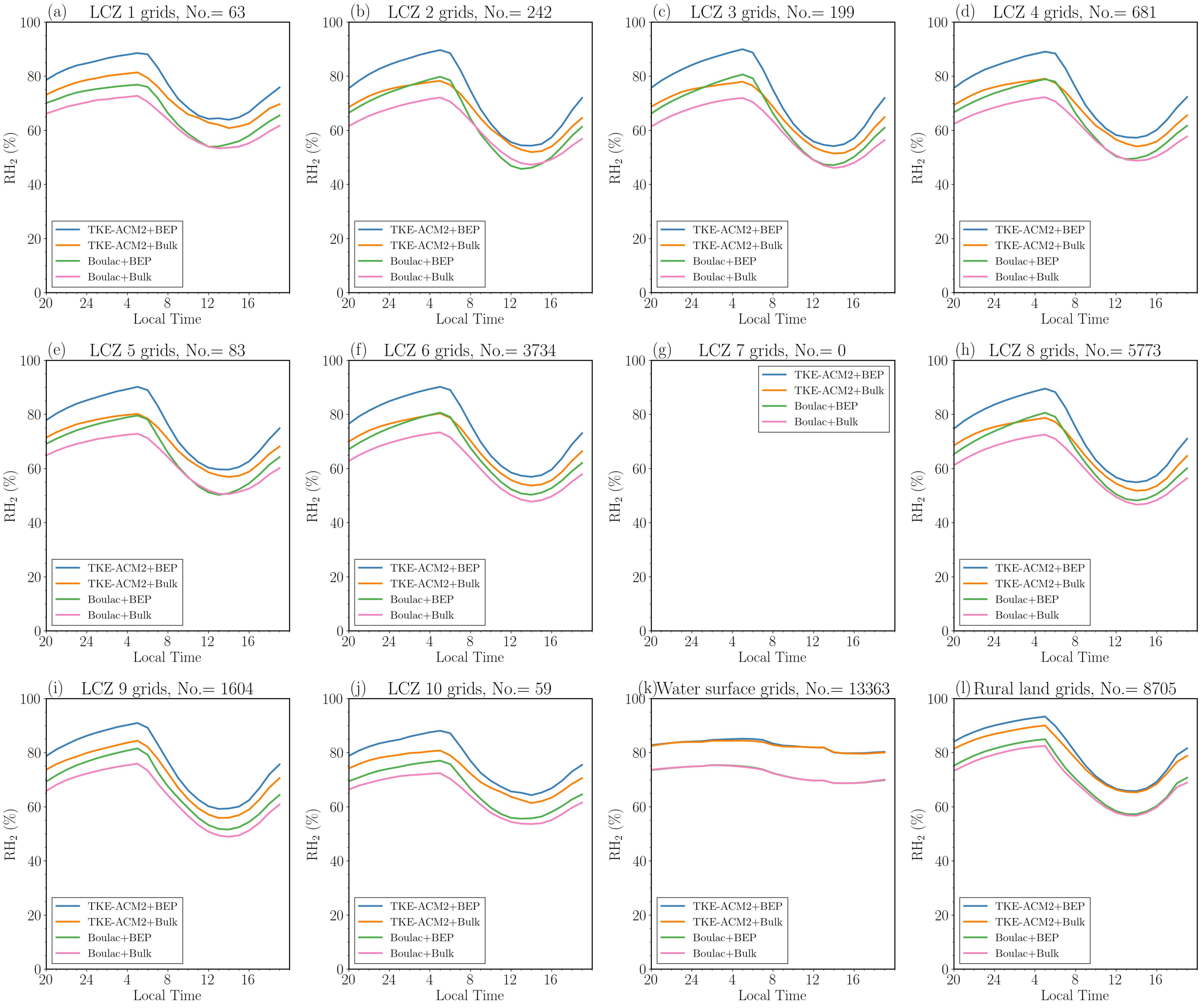

Figure C5. Same ~~to~~ as Fig.~~A3~~ C3 but for RH$_2$.

Author contributions. WZ: Conceptualization, methodology, data curation, validation, investigation, and formal analysis; RC and EYYN: Funding acquisition and project administration; MMFW: Methodology, data curation, and investigation; JCHF: Conceptualization, investigation, supervision, project administration, and funding acquisition. All authors reviewed and edited the manuscript.

Competing interests. The corresponding author declares that none of the authors has any competing interests.

Acknowledgements. We appreciate the assistance of the Hong Kong Observatory (HKO), which provided the meteorological data. The work described in this paper was supported by a grant from the Research Grants Council of the Hong Kong Special Administrative Region, China (Project Nos. C6026-22G and T31-603/21-N).

References

Arregocés, H. A., Rojano, R., and Restrepo, G.: Sensitivity analysis of planetary boundary layer schemes using the WRF model in Northern Colombia during 2016 dry season, Dynamics of Atmospheres and Oceans, 96, 101 261, https://doi.org/10.1016/j.dynatmoce.2021.101261, 2021.

Ayotte, K., Sullivan, P., Andren, A., Doney, S., Holtslag, B., Large, W., McWilliams, J., Moeng, C.-H., Otte, M., Tribbia, J., and Wyngaard, J.: An Evaluation of Neutral and Convective Planetary Boundary-Layer Parameterizations Relative to Large Eddy Simulations, Boundary-Layer Meteorology, 79, 131–175, https://doi.org/10.1007/BF00120078, 1996.

Banks, R. F., Tiana-Alsina, J., Baldasano, J. M., Rocadenbosch, F., Papayannis, A., Solomos, S., and Tzanis, C. G.: Sensitivity of boundary-layer variables to PBL schemes in the WRF model based on surface meteorological observations, lidar, and radiosondes during the HygrA-CD campaign, Atmospheric Research, 176-177, 185–201, https://doi.org/10.1016/j.atmosres.2016.02.024, 2016.

Bougeault, P. and Lacarrere, P.: Parameterization of Orography-Induced Turbulence in a Mesobeta–Scale Model, Monthly Weather Review, 117, 1872 – 1890, https://doi.org/10.1175/1520-0493(1989)117<1872:POOITI>2.0.CO;2, 1989.

Britter, R. E. and Hanna, S. R.: Flow and Dispersion in Urban Areas, Annual Review of Fluid Mechanics, 35, 469–496, https://doi.org/10.1146/annurev.fluid.35.101101.161147, _eprint: https://doi.org/10.1146/annurev.fluid.35.101101.161147, 2003.

Businger, J. A., Wyngaard, J. C., Izumi, Y., and Bradley, E. F.: Flux-Profile Relationships in the Atmospheric Surface Layer, Journal of Atmospheric Sciences, 28, 181–189, https://doi.org/10.1175/1520-0469(1971)028<0181:FPRITA>2.0.CO;2, place: Boston MA, USA Publisher: American Meteorological Society, 1971.

Chen, F. and Dudhia, J.: Coupling an Advanced Land Surface–Hydrology Model with the Penn State–NCAR MM5 Modeling System. Part I: Model Implementation and Sensitivity, Monthly Weather Review, 129, 569 – 585, https://doi.org/https://doi.org/10.1175/1520-0493(2001)129<0569:CAALSH>2.0.CO;2, 2001.

Chen, F., Kusaka, H., Bornstein, R., Ching, J., Grimmond, C. S. B., Grossman-Clarke, S., Loridan, T., Manning, K. W., Martilli, A., Miao, S., Sailor, D., Salamanca, F. P., Taha, H., Tewari, M., Wang, X., Wyszogrodzki, A. A., and Zhang, C.: The integrated WRF/urban modelling system: development, evaluation, and applications to urban environmental problems, International Journal of Climatology, 31, 273–288, https://doi.org/10.1002/joc.2158, _eprint: https://onlinelibrary.wiley.com/doi/pdf/10.1002/joc.2158, 2011.

Chen, X., Bryan, G. H., Hazelton, A., Marks, F. D., and Fitzpatrick, P.: Evaluation and Improvement of a TKE-Based Eddy-Diffusivity Mass-Flux (EDMF) Planetary Boundary Layer Scheme in Hurricane Conditions, Weather and Forecasting, 37, 935 – 951, https://doi.org/https://doi.org/10.1175/WAF-D-21-0168.1, place: Boston MA, USA Publisher: American Meteorological Society, 2022.

Cleugh, H. and Grimmond, S.: Chapter 3 - Urban Climates and Global Climate Change, in: The Future of the World's Climate (Second Edition), edited by Henderson-Sellers, A. and McGuffie, K., pp. 47–76, Elsevier, Boston, ISBN 978-0-12-386917-3, https://doi.org/10.1016/B978-0-12-386917-3.00003-8, 2012.

Coniglio, M. C., Correia, J., Marsh, P. T., and Kong, F.: Verification of Convection-Allowing WRF Model Forecasts of the Planetary Boundary Layer Using Sounding Observations, Weather and Forecasting, 28, 842 – 862, https://doi.org/10.1175/WAF-D-12-00103.1, 2013.

Davenport, A., Grimmond, S., Oke, T., and Wieringa, J.: Estimating the roughness of cities and sheltered country, 15th conference on probability and statistics in the atmospheric sciences/12th conference on applied climatology, Ashville, NC, American Meteorological Society, pp. 96–99, 2000.

Demuzere, M., Kittner, J., Martilli, A., Mills, G., Moede, C., Stewart, I. D., van Vliet, J., and Bechtel, B.: A global map of local climate zones to support earth system modelling and urban-scale environmental science, Earth System Science Data, 14, 3835–3873, https://doi.org/10.5194/essd-14-3835-2022, 2022.

Du, R., Liu, C.-H., Li, X.-X., and Lin, C.-Y.: Effect of local climate zone (LCZ) and building category (BC) classification on the simulation of urban climate and air-conditioning load in Hong Kong, Energy, 271, 127 004, https://doi.org/https://doi.org/10.1016/j.energy.2023.127004, 2023.

Gall, R., Franklin, J., Marks, F., Rappaport, E. N., and Toepfer, F.: The Hurricane Forecast Improvement Project, Bulletin of the American Meteorological Society, 94, 329 – 343, https://doi.org/https://doi.org/10.1175/BAMS-D-12-00071.1, 2013.

García-Díez, M., Fernández, J., Fita, L., and Yagüe, C.: Seasonal dependence of WRF model biases and sensitivity to PBL schemes over Europe, Quarterly Journal of the Royal Meteorological Society, 139, 501–514, https://doi.org/https://doi.org/10.1002/qj.1976, _eprint: https://rmets.onlinelibrary.wiley.com/doi/pdf/10.1002/qj.1976, 2013.

Hammerberg, K., Brousse, O., Martilli, A., and Mahdavi, A.: Implications of employing detailed urban canopy parameters for mesoscale climate modelling: A comparison between WUDAPT and GIS databases over Vienna, Austria, International Journal of Climatology, 38, https://doi.org/10.1002/joc.5447, 2018.

Hendricks, E. A., Knievel, J. C., and Wang, Y.: Addition of Multilayer Urban Canopy Models to a Nonlocal Planetary Boundary Layer Parameterization and Evaluation Using Ideal and Real Cases, Journal of Applied Meteorology and Climatology, 59, 1369 – 1392, https://doi.org/https://doi.org/10.1175/JAMC-D-19-0142.1, place: Boston MA, USA Publisher: American Meteorological Society, 2020.

Hong, S.-Y., Dudhia, J., and Chen, S.-H.: A Revised Approach to Ice Microphysical Processes for the Bulk Parameterization of Clouds and Precipitation, Monthly Weather Review, 132, 103 – 120, https://doi.org/https://doi.org/10.1175/1520-0493(2004)132<0103:ARATIM>2.0.CO;2, 2004.

Hong, S.-Y., Noh, Y., and Dudhia, J.: A New Vertical Diffusion Package with an Explicit Treatment of Entrainment Processes, Monthly Weather Review, 134, 2318–2341, https://doi.org/10.1175/MWR3199.1, 2006.

Hu, X.-M., Nielsen-Gammon, J. W., and Zhang, F.: Evaluation of Three Planetary Boundary Layer Schemes in the WRF Model, Journal of Applied Meteorology and Climatology, 49, 1831 – 1844, https://doi.org/https://doi.org/10.1175/2010JAMC2432.1, place: Boston MA, USA Publisher: American Meteorological Society, 2010.

Iacono, M. J., Delamere, J. S., Mlawer, E. J., Shephard, M. W., Clough, S. A., and Collins, W. D.: Radiative forcing by long-lived greenhouse gases: Calculations with the AER radiative transfer models, Journal of Geophysical Research: Atmospheres, 113, https://doi.org/https://doi.org/10.1029/2008JD009944, 2008.

Janjić, Z. I.: The Step-Mountain Eta Coordinate Model: Further Developments of the Convection, Viscous Sublayer, and Turbulence Closure Schemes, Monthly Weather Review, 122, 927–945, 1994.

Jiménez, P. A., Dudhia, J., González-Rouco, J. F., Navarro, J., Montávez, J. P., and García-Bustamante, E.: A Revised Scheme for the WRF Surface Layer Formulation, Monthly Weather Review, 140, 898 – 918, https://doi.org/https://doi.org/10.1175/MWR-D-11-00056.1, 2012.

Karlický, J., Huszár, P., Halenka, T., Belda, M., Žák, M., Pišoft, P., and Mikšovský, J.: Multi-model comparison of urban heat island modelling approaches, Atmospheric Chemistry and Physics, 18, 10 655–10 674, https://doi.org/10.5194/acp-18-10655-2018, 2018.

Kusaka, H. and Kimura, F.: Coupling a Single-Layer Urban Canopy Model with a Simple Atmospheric Model: Impact on Urban Heat Island Simulation for an Idealized Case, Journal of the Meteorological Society of Japan, 82, 67–80, https://api.semanticscholar.org/CorpusID:43081087, 2004.

Kusaka, H., Kondo, H., Kikegawa, Y., and Kimura, F.: A Simple Single-Layer Urban Canopy Model For Atmospheric Models: Comparison With Multi-Layer And Slab Models, Boundary-Layer Meteorology, 101, 329–358, https://doi.org/10.1023/A:1019207923078, 2001.

Kwok, Y. T., De Munck, C., Schoetter, R., Ren, C., and Lau, K.: Refined dataset to describe the complex urban environment of Hong Kong for urban climate modelling studies at the mesoscale, Theoretical and Applied Climatology, 142, https://doi.org/10.1007/s00704-020-03298-x, 2020.

Li, D.: Turbulent Prandtl number in the atmospheric boundary layer - where are we now?, Atmospheric Research, 216, 86–105, https://doi.org/10.1016/j.atmosres.2018.09.015, 2019.

Liu, Y., Chen, F., Warner, T., and Basara, J.: Verification of a Mesoscale Data-Assimilation and Forecasting System for the Oklahoma City Area during the Joint Urban 2003 Field Project, Journal of Applied Meteorology and Climatology, 45, 912 – 929, https://doi.org/https://doi.org/10.1175/JAM2383.1, place: Boston MA, USA Publisher: American Meteorological Society, 2006.

Lo, J. C. F., Lau, A. K. H., Chen, F., Fung, J. C. H., and Leung, K. K. M.: Urban Modification in a Mesoscale Model and the Effects on the Local Circulation in the Pearl River Delta Region, Journal of Applied Meteorology and Climatology, 46, 457 – 476, https://doi.org/https://doi.org/10.1175/JAM2477.1, place: Boston MA, USA Publisher: American Meteorological Society, 2007.

Makedonas, A., Carpentieri, M., and Placidi, M.: Urban Boundary Layers Over Dense and Tall Canopies, Boundary-Layer Meteorology, 181, 73–93, https://doi.org/10.1007/s10546-021-00635-z, 2021.

Maronga, B., Gryschka, M., Heinze, R., Hoffmann, F., Kanani-Sühring, F., Keck, M., Ketelsen, K., Letzel, M. O., Sühring, M., and Raasch, S.: The Parallelized Large-Eddy Simulation Model (PALM) version 4.0 for atmospheric and oceanic flows: model formulation, recent developments, and future perspectives, Geoscientific Model Development, 8, 2515–2551, https://doi.org/10.5194/gmd-8-2515-2015, 2015.

Martilli, A., Clappier, A., and Rotach, M. W.: An Urban Surface Exchange Parameterisation for Mesoscale Models, Boundary-Layer Meteorology, 104, 261–304, https://doi.org/10.1023/A:1016099921195, 2002.

Martilli, A., Grossman-Clarke, S., Tewari, M., and Manning, K. W.: Description of the Modifications Made in WRF.3.1 and Short User's Manual of BEP, 2009.

Nazarian, N., Krayenhoff, E. S., and Martilli, A.: A one-dimensional model of turbulent flow through "urban" canopies (MLUCM v2.0): updates based on large-eddy simulation, https://doi.org/10.5194/gmd-13-937-2020, 2020.

Olson, J. B., Kenyon, J. S., Angevine, W. A., Brown, J. M., Pagowski, M., and Sušelj, K.: A Description of the MYNN-EDMF Scheme and the Coupling to Other Components in WRF–ARW, https://doi.org/10.25923/n9wm-be49, 2019.

Pappaccogli, G., Giovannini, L., Zardi, D., and Martilli, A.: Assessing the Ability of WRF-BEP + BEM in Reproducing the Wintertime Building Energy Consumption of an Italian Alpine City, Journal of Geophysical Research: Atmospheres, 126, e2020JD033 652, https://doi.org/https://doi.org/10.1029/2020JD033652, _eprint: https://agupubs.onlinelibrary.wiley.com/doi/pdf/10.1029/2020JD033652, 2021.

Pleim, J. E.: A Combined Local and Nonlocal Closure Model for the Atmospheric Boundary Layer. Part II: Application and Evaluation in a Mesoscale Meteorological Model, Journal of Applied Meteorology and Climatology, 46, 1396–1409, https://doi.org/10.1175/JAM2534.1, 2007a.

Pleim, J. E.: A Combined Local and Nonlocal Closure Model for the Atmospheric Boundary Layer. Part I: Model Description and Testing, Journal of Applied Meteorology and Climatology, 46, 1383–1395, https://doi.org/10.1175/JAM2539.1, 2007b.

Raasch, S. and Schröter, M.: PALM-A large-eddy simulation model performing on massively parallel computers, Meteorologische Zeitschrift, 10, 363–372, https://doi.org/10.1127/0941?2948/2001/0010?0363, 2001.

Ribeiro, I., Martilli, A., Falls, M., Zonato, A., and Villalba, G.: Highly resolved WRF-BEP/BEM simulations over Barcelona urban area with LCZ, Atmospheric Research, 248, 105 220, https://doi.org/10.1016/j.atmosres.2020.105220, 2021.

Rotach, M.: Turbulence close to a rough urban surface part I: Reynolds stress, Boundary-Layer Meteorology, 65, 1–28, https://doi.org/10.1007/BF00708816, 1993.

Rotach, M. W.: On the in#uence of the urban roughness sublayer on turbulence and dispersion, Atmospheric Environment, 1999.

Rotach, M. W.: Simulation Of Urban-Scale Dispersion Using A Lagrangian Stochastic Dispersion Model, Boundary-Layer Meteorology, 99, 379–410, https://doi.org/10.1023/A:1018973813500, 2001.

Roth, M.: Review of atmospheric turbulence over cities, Quarterly Journal of the Royal Meteorological Society, 126, 941–990, https://doi.org/https://doi.org/10.1002/qj.49712656409, _eprint: https://rmets.onlinelibrary.wiley.com/doi/pdf/10.1002/qj.49712656409, 2000.

Salamanca, F. and Martilli, A.: A new Building Energy Model coupled with an Urban Canopy Parameterization for urban climate simulations—part II. Validation with one dimension off-line simulations, Theoretical and Applied Climatology, 99, 345–356, https://doi.org/10.1007/s00704-009-0143-8, 2010.

Schmidt, H. and Schumann, U.: Coherent structure of the convective boundary layer derived from large-eddy simulations, Journal of Fluid Mechanics, 200, 511–562, https://doi.org/10.1017/S0022112089000753, 1989.

Shen, C., Chen, X., Dai, W., Li, X., Wu, J., Fan, Q., Wang, X., Zhu, L., Chan, P., Hang, J., Fan, S., and Li, W.: Impacts of High-Resolution Urban Canopy Parameters within the WRF Model on Dynamical and Thermal Fields over Guangzhou, China, Journal of Applied Meteorology and Climatology, 58, 1155–1176, https://doi.org/10.1175/JAMC-D-18-0114.1, place: Boston MA, USA Publisher: American Meteorological Society, 2019.

Shin, H. H. and Dudhia, J.: Evaluation of PBL Parameterizations in WRF at Subkilometer Grid Spacings: Turbulence Statistics in the Dry Convective Boundary Layer, Monthly Weather Review, 144, 1161–1177, https://doi.org/10.1175/MWR-D-15-0208.1, place: Boston MA, USA Publisher: American Meteorological Society, 2016.

Skamarock, W. C., Klemp, J. B., Dudhia, J., Gill, D. O., Liu, Z., Berner, J., Wang, W., Powers, J. G., Duda, M. G., and Barker, D. M.: A description of the advanced research WRF model version 4, National Center for Atmospheric Research: Boulder, CO, USA, 145, 550, 2019.

Sun, Y., Zhang, N., Miao, S., Kong, F., Zhang, Y., and Li, N.: Urban Morphological Parameters of the Main Cities in China and Their Application in the WRF Model, Journal of Advances in Modeling Earth Systems, 13, e2020MS002 382, https://doi.org/10.1029/2020MS002382, publisher: John Wiley & Sons, Ltd, 2021.

Wang, J. and Hu, X.-M.: Evaluating the Performance of WRF Urban Schemes and PBL Schemes over Dallas–Fort Worth during a Dry Summer and a Wet Summer, Journal of Applied Meteorology and Climatology, 60, 779 – 798, https://doi.org/https://doi.org/10.1175/JAMC-D-19-0195.1, place: Boston MA, USA Publisher: American Meteorological Society, 2021.

Wang, Y., Di Sabatino, S., Martilli, A., Li, Y., Wong, M. S., Gutiérrez, E., and Chan, P. W.: Impact of land surface heterogeneity on urban heat island circulation and sea-land breeze circulation in Hong Kong, Journal of Geophysical Research: Atmospheres, 122, 4332–4352, https://doi.org/https://doi.org/10.1002/2017JD026702, _eprint: https://agupubs.onlinelibrary.wiley.com/doi/pdf/10.1002/2017JD026702, 2017.

Xie, B. and Fung, J. C. H.: A comparison of momentum mixing models for the planetary boundary layer, Journal of Geophysical Research: Atmospheres, 119, 2079–2091, https://doi.org/https://doi.org/10.1002/2013JD020273, _eprint: https://agupubs.onlinelibrary.wiley.com/doi/pdf/10.1002/2013JD020273, 2014.

Xie, B., Fung, J. C. H., Chan, A., and Lau, A.: Evaluation of nonlocal and local planetary boundary layer schemes in the WRF model, Journal of Geophysical Research: Atmospheres, 117, https://doi.org/10.1029/2011JD017080, _eprint: https://onlinelibrary.wiley.com/doi/pdf/10.1029/2011JD017080, 2012.

Zhang, W.: Supplementary, raw data, and model for manuscript titled Coupling the TKE-ACM2 Planetary Boundary Layer Scheme with the Building Effect Parameterization Model [Data set], https://doi.org/10.5281/zenodo.13959540, 2024.

Zhang, W., Fung, J. C. H., and Wong, M. M. F.: An Improved Non-Local Planetary Boundary Layer Parameterization Scheme in Weather Forecasting and Research Model Based on a 1.5-Order Turbulence Closure Model, Journal of Geophysical Research: Atmospheres, 129, e2023JD040 432, https://doi.org/10.1029/2023JD040432, publisher: John Wiley & Sons, Ltd, 2024.

Zonato, A., Martilli, A., Jimenez, P. A., Dudhia, J., Zardi, D., and Giovannini, L.: A New K–epsilon Turbulence Parameterization for Mesoscale Meteorological Models, Monthly Weather Review, 150, 2157 – 2174, https://doi.org/https://doi.org/10.1175/MWR-D-21-0299.1, place: Boston MA, USA Publisher: American Meteorological Society, 2022.